Title

Deficiency in a special dynein DNAH12 causes male infertility by impairing DNAH1 and DNALI1 recruitment in humans and mice

Authors

Menglei Yang[1], Hafiz Muhammad Jafar Hussain[1], Manan Khan[1], Zubair Muhammad[1], Jianteng Zhou[1], Ao Ma[1], Xiongheng Huang[1], Jingwei Ye[1], Min Chen[1], Aoran Zhi[1], Tao Liu[1], Ranjha Khan[1], Asim Ali[1], Wasim Shah[1], Aurang Zeb[1], Nisar Ahmad[1], Huan Zhang[1], Bo Xu[1], Hui Ma[1]*, Qinghua Shi[1]*, Baolu Shi[1]*

Affiliations

1. Center for Reproduction and Genetics, First Affiliated Hospital of USTC, Hefei National Research Center for Physical Sciences at the Microscale, the CAS Key Laboratory of Innate Immunity and Chronic Disease, School of Basic Medical Sciences, Division of Life Sciences and Medicine, Biomedical Sciences and Health Laboratory of Anhui Province, Institute of Health and Medicine, Hefei Comprehensive National Science Center, University of Science and Technology of China, Hefei 230027, China.

*Correspondence:

bl625@ustc.edu.cn (B.S.), qshi@ustc.edu.cn (Q.S.), clsmh@ustc.edu.cn (H.M.)

Abstract

Asthenoteratozoospermia, a prevalent cause of male infertility, lacks a well-defined etiology. DNAH12 is a special dynein featured by the absence of a microtubule-binding domain, however, its functions in spermatogenesis remain largely unknown. Through comprehensive genetic analyses involving whole-exome sequencing and subsequent Sanger sequencing on infertile patients and fertile controls from six distinct families, we unveiled six biallelic mutations in *DNAH12* that co-segregate recessively with male infertility in the studied families. Transmission electron microscopy (TEM) revealed pronounced axonemal abnormalities, including inner dynein arms (IDAs) impairment and central pair (CP) loss in sperm flagella of the patients. Mouse models (*Dnah12*$^{-/-}$ and *Dnah12*$^{mut/mut}$) were generated and recapitulated the reproductive defects in the patients. Noteworthy, DNAH12 deficiency did not show effects on cilium organization and function. Mechanistically, DNAH12 was confirmed to interact with two other IDA components DNALI1 and DNAH1, while disruption of DNAH12 leads to failed recruitment of DNALI1 and DNAH1 to IDAs and compromised sperm development. Furthermore, DNAH12 also interacts with radial spoke head proteins RSPH1, RSPH9, and DNAJB13 to regulate CP stability. Moreover, the infertility of *Dnah12*$^{-/-}$ mice could be overcome by intracytoplasmic sperm injection (ICSI) treatment. Collectively, DNAH12 plays a crucial role in the proper organization of axoneme in sperm flagella, but not cilia, by recruiting DNAH1 and DNALI1 in both humans and mice. These findings expand our comprehension of dynein component assembly in flagella and cilia and provide a valuable marker for genetic counseling and diagnosis of asthenoteratozoospermia in clinical practice.

Keywords

male infertility; DNAH12; knockout mice; inner dynein arms assembly; flagella and cilia; flagellar development

Introduction

Infertility has emerged as a global health concern, impacting around 8-12% of couples during their reproductive years, approximately 50% of infertility cases are attributed to male factors (1). Among these, asthenoteratozoospermia, characterized by poor sperm motility and notable morphological abnormalities, stands out as a prevalent contributor to male infertility (2, 3). Recent investigations have unveiled a multitude of gene mutations associated with asthenoteratozoospermia and male infertility, including Dynein Axonemal Heavy Chain (DNAH) inner dynein arm (IDA) genes like *DNAH1, DNAH2, DNAH6, DNAH7,* and *DNAH10*, as well as outer dynein arm (ODA) genes such as *DNAH8* and *DNAH17*, all implicated in primary male infertility with asthenoteratozoospermia (4-11). Additionally, genes encoding cilia and flagella-associated proteins (CFAP), including *CFAP43*, *CFAP44*, *CFAP57*, and *CFAP61*, have been identified as linked to asthenoteratozoospermia (12-15). Despite these advances, the intricate and heterogeneous features of asthenoteratozoospermia leave a significant number of cases unexplained. It is anticipated that additional genetic factors play a role in sperm anomalies and dysfunction.

The axoneme, a fundamental structure of cilia and flagella, exhibits a well-organized pattern with nine peripheral doublet microtubules (DMTs) and a central pair of microtubules (CP), constituting the classical “9+2” microtubular arrangement (16). In motile cilia or flagella, the radial spoke (RS) head contacts the CP accessory structures, transmitting mechanical and chemical signals from the central microtubules to the axonemal dynein arms, thus coordinating the flagellar or ciliary movement (17).

Within mammalian species, the DNAH family plays a crucial role in the axonemal structure, encompassing eight IDA members (DNAH1-3, DNAH6, DNAH7, DNAH10, DNAH12, DNAH14) and five ODA members (DNAH5, DNAH8, DNAH9, DNAH11, DNAH17). Despite the collaborative effort of IDAs and ODAs in generating the force necessary for flagellar and ciliary motion, they serve distinct functions. Chlamydomonas ODAs, composed of α, β, and γ chains, primarily regulate beat frequency, while IDAs, with seven major subspecies (a-g), contribute to bending formation and beating form (18). Mutations in genes encoding ODA or IDA components have been linked to asthenoteratozoospermia, with or without symptoms of primary ciliary dyskinesia (PCD), a genetic disorder characterized by chronic airway infections or situs inversus (19). Notably, deficiency in certain IDAs and ODAs coding genes, such as *DNAH7* or *DNAH11*, may lead to PCD (20-22). Patients carrying mutations in *DNAH1* and *DNAH2* typically lack PCD symptoms (4, 23), although a study suggested the potential contribution of the DNAH1 p.Lys1154Gln mutation to PCD (24). The extensive genetic heterogeneity and clinical variabilities underscore the intricacy and uniqueness of dynein arms in flagella and cilia. However, the susceptibility of uncharacterized dynein factors that related to asthenoteratozoospermia and/or PCD remains unclear, given the absence of human genetic evidence or corresponding animal models.

Dynein axonemal heavy chain 12, DNAH12 (MIM: 603340, GenBank: NM_001366028.2), also known as DHC3, is a unique dynein arm component (25). Notably, it is the shortest member and lacks a typical microtubule-binding domain (MTBD) in the DNAH family. Mutations of *DNAH12* have been predicted to be associated with male patients' infertility, however, limited pathogenic evidence was provided, and the underlying pathogenesis remained unclear (26, 27). Besides, although DNAH12 has been identified as a possible axonemal dynein and its mRNA is predominantly detected in two tissues containing axonemal structures: trachea and testis (25, 28), its physiological functions remain largely elusive.

In this study, we enrolled 796 infertile patients from unrelated Pakistani and Chinese families diagnosed with asthenozoospermia. Utilizing whole-exome sequencing (WES) followed by Sanger sequencing, we identified six novel bi-allelic mutations in *DNAH12* in infertile males from six unrelated families. All these mutations resulted in the loss of DNAH12 protein in the sperm of patients. Two mouse models, *Dnah12*$^{-/-}$ and *Dnah12*$^{mut/mut}$, were generated and exhibited asthenoteratozoospermia and male infertility, mimicking our patients' phenotypes. Deficiency in DNAH12 led to axoneme defects characterized by impaired IDAs and CP loss in sperm flagella, while no such defects were observed in cilia. DNAH12 interacts with other IDA components like DNALI1 and DNAH1 in mouse testes, and disruption of DNAH12 impaired the recruitment of dynein components into sperm flagella. Our findings unveil, for the first time, that DNAH12 plays a pivotal role in facilitating the recruitment of IDA components specifically in flagella, but not in cilia. Furthermore, we demonstrate that bi-allelic mutations in *DNAH12* are identified as causative factors for asthenoteratozoospermia and male infertility in both humans and mice. These results enhance our understanding of the development of axonemal structures in flagella versus cilia and provide valuable clues for genetic counseling and future individualized treatment for infertile males carrying *DNAH12* mutations in clinical practice.

Materials and methods

Human subjects

Informed consent and peripheral blood were obtained from the participants and the patients' information

103 was registered in the Human Reproductive Disease Resource Bank database. Sperm analyses were
104 performed according to the WHO guidelines (29). During their medical consultation, all patients
105 answered a questionnaire regarding clinical presentations. This study was approved by the institutional
106 ethics committee of University of Science and Technology of China (USTC) with the approval number
107 2019-KY-168.

108 **Whole exome sequencing (WES) and bioinformatics analyses**

109 Whole-exome capture and sequencing were performed by capturing exons from genomic DNAs of
110 peripheral blood cells, using the SureSelect XT 50 Mb Exon Capture Kit (Agilent, California, USA), and
111 then high-throughput sequencing was conducted on the HiSeq 2000 platform (Illumina, San Diego, CA,
112 USA) following instructions. Variants were called using the Genome Analysis Toolkit HaplotypeCaller
113 and annotated through ANNOVAR (30). Variants within exons or exon-intron boundaries were retained
114 and filtered through the criteria we previously described (31). Bcftools was applied to detect runs of
115 homozygosity (32). Runs of homozygosity over 1.5 Mb were used to calculate the inbreeding coefficients.
116 The genotypes were validated using Sanger sequencing validation. Additional primers are listed in
117 Supplemental Table 1. For phylogenetic analysis, different DNAH12 protein sequences were extracted
118 from the UniProt database, and the sequence alignment and phylogenetic tree construction were
119 generated using MEGA11 (33). Newick format tree files were extracted and processed in the Evolview
120 v2 tool (34). For gene family and conserved domain analyses, the batch sequence search tool in Pfam
121 was used to analyze features of proteins and further visualized with the assistance of Evolview v2 tool
122 and TBtools (35, 36). For protein structure analysis, the structure models were predicted and constructed
123 with the Phyre2 tool (37), interactions were analyzed by the HDOCK (http://hdock.phys.hust.edu.cn/)
124 and Alphafold3 (https://golgi.sandbox.google.com/). The predicted protein structures and possible
125 interactions were further explored and visualized by UCSF Chimera (Version: 1.15, California, USA)
126 according to the manual instruction (38).

127 **Scanning electron microscopy (SEM) and Transmission electron microscopy (TEM)**

128 Fresh semen samples were obtained and centrifuged at 900 g for 3 min. Spermatozoa were washed with
129 phosphate buffer saline (PBS) three times. Then the sediment was fixed in 0.1 M phosphate buffer (pH
130 7.4) containing 4% paraformaldehyde, 8% glutaraldehyde, and 0.2% picric acid at 4°C for at least 8
131 hours. Scanning electron microscopy (SEM) and Transmission electron microscopy (TEM) were then
132 conducted as we previously described (39).

133 **Generation and verification of the polyclonal anti-DNAH12 antibody**

134 The characteristics of the DNAH12 were analyzed and the 1-200 amino acids sequence of mouse
135 DNAH12 protein (UniProt accession no. Q69Z23) was regarded as the ideal antigen for immunization.
136 Subsequently, the DNAH12 polyclonal antibody was generated in rabbits and rats using the mentioned
137 peptide by Dia-An Biotech, Inc., in Wuhan, China. The specificity of antibodies was further validated
138 using *Dnah12*$^{+/+}$ and *Dnah12*$^{-/-}$ mice in this study.

139 **Immunoblotting**

140 Protein lysate was prepared as we previously described (40, 41). Tissues or cells were lysed using lysis
141 buffer (50 mM tris (pH 7.5), 150 mM NaCl, 5 mM EDTA, and 0.1% NP-40). For human sperm cells,
142 proteins were extracted using the TRIzol reagent. The protein sediment was washed with 95% ethanol
143 containing 0.3M guanidine hydrochloride, dissolved in 1% SDS. Then the protein lysate was boiled for
144 10 minutes, and diluted in SDS-sample buffer (120 mM Tris/HCl, 10% SDS, 20% glycerol, 20% 2-
145 mercaptoethanol, and bromophenol blue (pH 6.8). Whereafter the proteins were separated by SDS-PAGE
146 and transferred onto nitrocellulose blotting membranes with a pore size of 0.45 μm (GE Healthcare,

147 10600002). The membranes were blocked with TBS-Tween buffer (50 mM Tris, 150 mM NaCl, and 0.5%
148 Tween-20, pH 7.4) containing 5% skim milk for 30 minutes to reduce unspecific binding and then
149 incubated with primary antibodies diluted in TBST buffer containing 5% skim milk at 4°C overnight.
150 Incubation with secondary antibodies for 1.5 hours was followed by chemiluminescence development
151 system (GE Healthcare, Pittsburgh, USA). Antibodies details are listed in Supplemental Table 2-3.

152 **Immunofluorescence (IF) staining**

153 Human semen smear slides were prepared following the guidelines of WHO (29). Mouse sperm smear
154 slide preparation and immunofluorescence staining were conducted as we described (42). For tissue IF
155 staining, tissues were collected and fixed in 4% paraformaldehyde (PFA), the 5μm tissue sections were
156 deparaffinized in xylene, rehydrated in a graded series of ethanol (100%, 95%, 90%, 80%, 70%, and 50%
157 ethanol) and sterile water, and permeabilized with 0.2% Triton X-100 in PBS for 30min. Antigen retrieval
158 was then conducted by boiling slides in a microwave for 30 minutes in 10 mM citrate buffer (pH 6.0).
159 The other steps are consistent with sperm IF staining. Images of spermatozoa were captured using a
160 Nikon ECLIPSE 80i microscope equipped with a charge-coupled device (Hamamatsu Photonics,
161 Hamamatsu, Japan). Information of antibodies is available in Supplemental Table 2-3**.**

162 **Animal models and fertility test**

163 Two mouse models (*Dnah12*$^{-/-}$ and *Dnah12*$^{mut/mut}$) were generated using CRISPR/Cas9 Technology (43).
164 Briefly, to generate the *Dnah12*$^{-/-}$ mouse model, guide RNAs (gRNAs) targeting exon 5 of *Dnah12*, a key
165 exon shared by all its transcripts, were transcribed in vitro (Thermo Fisher, CA, USA). Then, the gRNAs
166 and the Cas9 protein were electroporated into C57BL/6 mouse zygotes. The zygotes were introduced
167 into ICR female mice, and the genotypes of the pups were checked using Polymerase Chain Reaction
168 (PCR) with designed primers. Similar conductions were performed targeting exon 18 of *Dnah12* to
169 generate the *Dnah12*$^{mut/mut}$ mice. The genotyping primers are listed in Supplemental Table 1. For male
170 fertility test, each 8-10 weeks male mouse was caged with wild-type female mice; for female fertility
171 test, each 8-10 weeks female mouse was caged with one 8-10 weeks *Dnah12*$^{+/-}$ male mouse, the number
172 of offspring was recorded.

173 **Reverse-transcription PCR and real-time quantitative PCR**

174 For reverse-transcription PCR (RT-PCR), total RNA was extracted from mouse tissues using TRIzol
175 reagent (TAKARA, Japan). Whereafter 1μg of RNA was reverse-transcribed using the PrimeScript RT
176 Reagent Kit (TAKARA, Japan). The cDNA was diluted to a comparable concentration and then used for
177 RT–PCR. All amplified DNA fragments were visualized by 2% agarose gel electrophoresis containing
178 GelRed (APExBIO, Houston, TX, USA). For real-time quantitative PCR (qPCR), the experiments were
179 performed by using Hieff UNICON® Universal Blue qPCR SYBR Green Master Mix reagent (Yeasen
180 Biotechnology, Shanghai, China) on CFX96® Real-Time System (Bio-Rad, CA, USA) according to the
181 manufacturer's guidelines. Details of the primers were listed in Supplemental Table 1.

182 **Histological analysis**

183 As previously described (31), after sacrificing mice, the testes, epididymides, tracheas, and oviducts were
184 harvested and fixed in Bouin's fixative solution (Sigma–Aldrich, Missouri, USA) for hematoxylin and
185 eosin (H&E) staining or 4% PFA fixative solution for immunofluorescence or TUNEL assay. The pictures
186 were captured using a microscope equipped with a charge-coupled device camera (Nikon, Tokyo, Japan).

187 **Sperm counts, motility and morphology analysis**

188 As previously described (44), H&E staining or Papanicolaou staining kit (Solabio, Beijing, China) was
189 used for the evaluation of sperm morphology of patients. For mouse sperm parameters analysis, 8-10-
190 week-old mice were sacrificed by cervical dislocation, the sperm number per epididymis was then

191 assessed by cutting the epididymis into pieces in PBS and incubating them for 30 minutes at 37°C to
192 release the sperm, then counting with a hemocytometer. Sperm motility were assessed by computer-aided
193 sperm analysis (CASA) as we described (14). Sperm morphology was assessed on sperms collected from
194 epididymal cauda after H&E staining.

195 **Testicular cell smear slides and seminiferous tubule squash slides preparation**

196 To prepare testicular cell smears, mice were sacrificed and testes were then detached with one time of
197 PBS washing. Then testes were peeled off the testicular capsule, torn into small pieces, and then cut into
198 tiny pieces in PBS. Finally, the cell suspension was filtered through a 200-mesh cell strainer, the filtered
199 cell suspensions were added 10% FBS before spread onto glass slides. For testicular seminiferous tubule
200 squash slide preparation, the testes were dissected and carefully isolated into single testicular
201 seminiferous tubules in PBS dishes. After 10 mins of prefixation in fix/lysis solution (2% PFA, 50%
202 PBS), we then applied 100μL fix/lysis solution onto poly-L-lysine coated glass slides and carefully teased
203 apart approximately 20 seminiferous tubules with the assistance of 2 sterile forceps on the slides. After
204 that, coverslips were applied using slide forceps and pressed with the heel of the palm for 10 seconds,
205 then the glass slides were frozen in a small container with liquid N_2 immediately till the liquid ceases to
206 bubble. The slides were saved in the -80°C fridge keeping the coverslip on the slides or removing
207 coverslips for immunofluorescence staining.

208 **TUNEL assay**

209 As previously described (44), In Situ Cell Death Detection Kit, Fluorescein (Sigma–Aldrich, Missouri,
210 USA) was applied according to the manufacturer's protocol. Images were captured using a Nikon Eclipse
211 80i microscope equipped with Hamamatsu C4742-80 digital camera and analyzed using the NIS-Element
212 Microscope imaging software (Nikon, Tokyo, Japan).

213 **Cell culture and transfection.**

214 As previously described (40), HEK293T (ATCC, VA, USA) cells were cultured to 70%-80% density in
215 12-well plates, followed by transfected with plasmids expressing mCherry-tagged mouse DNAH12 and
216 GFP-tagged mouse DNALI1 using Lipofectamine 3000 (Thermo Fisher, CA, USA) according to the
217 manufacturer's instructions. Cells were harvested for in-vitro IP and immunoblotting the next day after
218 transfection. The sequences of the primers for plasmid construction are listed in Supplemental Table 4.

219 **Co-immunoprecipitation (Co-IP)**

220 Tissue extracts were prepared using lysis buffer supplemented with PMSF, Protease Inhibitor Cocktail
221 (Solarbio, Beijing, China) on ice using a glass homogenizer. Lysate was then centrifuged at 12,000 g at
222 4°C for 10 min, and the supernatant was divided into equal aliquots. Each aliquot was incubated with 1.5
223 μg of target antibody or rabbit IgG nonspecific antibody. After incubation at 4°C overnight with rotation,
224 beads were washed five times with lysis buffer. Finally, the beads were resuspended in SDS-sample
225 buffer and boiled at 100°C for 10 min. The samples were either analyzed by immunoblotting immediately
226 or stored at -80°C. For Co-IP in cultured cells, HEK293T cells were plated in six-well plates, followed
227 by transfection using Lipofectamine 3000 reagents. MG132 was added into the cultured cells 6 hours
228 before cell harvesting. Cells were washed with PBS for 10 min, cells were then collected and lysed in
229 the same lysis buffer used for Co-IP from testicular samples. The cell lysate was then incubated with
230 prewashed Magnetic Beads (Bimake, Texas, USA) and primary antibodies at 4°C overnight, followed by
231 washing and boiling as described above for the Co-IP protocols for testicular samples.

232 **Mass spectrometry proteomics**

233 To identify potential partners that interact with DNAH12, we performed in vivo IP of mouse testes lysate.
234 Tissue extracts were prepared using lysis buffer supplemented with PMSF, Protease Inhibitor Cocktail

235 (Solarbio, Beijing, China) with the same operation of the Co-IP protocol. Beads were washed 3 times
236 with lysis buffer and 3 times with 50 mM NH_4HCO_3, the pull-down proteins were digested with 0.2μg
237 Trypsin overnight and stopped by 5% Formic acid, (Thermo Fisher, CA, USA). The peptide mixture was
238 then desalted, dried with a SpeedVac, and resuspended in 0.1% Formic acid, followed by the MS analysis
239 using timsTOF Pro 2 mass spectrometer (Bruker, Massachusetts, USA). The proteomics data are
240 available on the ProteomeXchange Consortium via the iProX partner repository (45), with the dataset
241 identifier PXD051681.

242 **Intracytoplasmic sperm injection (ICSI)**

243 3.5-4-week-old female mice were given an intraperitoneal injection of 5 IU Pregnant Mare Serum
244 Gonadotropin (PMSG, Ningbo Sansheng, China). After 48 hours, a second intraperitoneal injection of 5
245 IU human Chorionic Gonadotropin (hCG, Ningbo Sansheng, China) was administered. The mice were
246 euthanized by cervical dislocation after 15 hours post-hCG injection. The oviducts were excised and the
247 ampullary regions were opened to release the cumulus-oocyte complexes (COCs). The cumulus cells
248 surrounding the oocytes were digested using hyaluronidase, and the morphologically round MII stage
249 oocytes were selected and washed three times in M2 medium (Sigma–Aldrich, Missouri, USA) before
250 being set aside for use. Male mice are euthanized by cervical dislocation, the epididymides are excised
251 and gently punctured with a syringe, allowing the spermatozoa to flow out. The spermatozoa were then
252 placed in the human tubal fluid (HTF) medium (EasyCheck, Nanjing Aibei Biotechnology, China) and
253 then frozen and thawed repeatedly to remove sperm tails, the single sperm head was microinjected into
254 an MII oocyte and then cultured in potassium simplex optimized medium (KSOM, EasyCheck, Nanjing
255 Aibei Biotechnology, China) at 37 °C under 5% CO_2.

256 **Statistics analysis**

257 Statistical analyses were performed using GraphPad Prism 8.0 (GraphPad Software, San Diego, CA,
258 USA). Values in tables and graphs are expressed as mean ± SEM. Two groups of mice were compared
259 with Student's 2-tailed t-test for independent data and $P > 0.05$ was considered not significant (ns); *$P <$
260 0.05, **$P < 0.01$, ***$P < 0.001$, and ****$P < 0.0001$ were considered significant.

261

262 **Results**

263 **Identification of biallelic *DNAH12* variants in men with asthenoteratozoospermia**

264 To identify the genetic factors contributing to male infertility, we recruited patients with primary
265 infertility and their family members from Pakistan and China. WES was performed on these individuals,
266 followed by comprehensive analyses of the WES data (Supplemental Figure 1, A-D). Seven mutations
267 in *DNAH12* were identified as potential pathogenic factors for male infertility in patients P1-3 of family
268 1, P4-5 of family 2, P8 of family 3, and P9, P10, and P11, all of whom suffered from
269 asthenoteratozoospermia (Fig. 1A). Initially, a homozygous frameshift mutation c.944_945 del (p.
270 Phe315*) in family 1, and two homozygous missense mutations, c. A164G (p. Gln55Arg) in family 2
271 and c. A2560G (p. Ile854Val) in family 3, were identified in *DNAH12* as potential causes of infertility.
272 Subsequently, four other mutations in *DNAH12* were discovered in three sporadic Chinese patients with
273 asthenoteratozoospermia: a homozygous stop-gain mutation c.2680 C>T (p. Gln2077*) in subject P9, a
274 homozygous missense mutation c.2813T>C (p. Val938Ala) in P10, and compound heterozygous
275 mutations c.2680C>T (p. Arg894Cys) and c.5964-3A>G in P11 (Fig. 1A and B).

276 All seven variants were rare in public human genome databases, including the 1000 Genome Project
277 and gnomAD (v3). Additionally, these variants were predicted to be deleterious by in-silico software

278 tools such as SIFT, Polyphen2, fathmm-MKL, and CADD2 (Table 1). Sanger Sequencing further
279 validated these variants and revealed the recessive pathogenic pattern of these mutations (Fig. 1A).
280 Collectively, these results suggested that the identified bi-allelic *DNAH12* variants could potentially be
281 the cause of asthenoteratozoospermia in our patients.

282 **DNAH12 protein is conserved in mammals and highly expressed in the testes**

283 *DNAH12* encodes a functionally uncharacterized protein and is predicted to be abundantly expressed in
284 testes of humans and mice based on our bioinformatics tool FertilityOnline (46). Experimentally, our RT-
285 PCR, qPCR, and immunoblotting detection of DNAH12 expression in different tissues indicated that
286 both DNAH12 mRNA and protein showed high expression in testes and relatively lower expression in
287 lungs and tracheas of male mice and oviducts of female mice (Supplemental Figure 2, A-C). It's worth
288 noting that in epididymides, DNAH12 protein, but not mRNA, was detected, indicating the DNAH12
289 protein detected in epididymides is from testes, most probably from sperm. Furthermore, DNAH12
290 protein was initially detected in testes around 21 days postpartum (dpp) and thereafter maintained a high
291 level (Supplemental Figure 2D). The expression pattern of DNAH12 in testes suggests that it is possibly
292 involved in spermiogenesis, and its abnormal expression could lead to asthenozoospermia or
293 asthenoteratozoospermia, further indicating that the identified *DNAH12* mutations are candidate
294 pathogenic mutations for patients.

295 Further phylogenetic analysis revealed the conservative nature of DNAH12 from Chlamydomonas
296 to humans (Supplemental Figure 3). All the amino acids affected by mutations were conserved in
297 mammals and were located in functional regions, including the ATPase domains or the Stem domain of
298 DNAH12 **(**Fig.1C), indicating that these mutations are highly likely to hinder the structure, function, or
299 stability of the DNAH12 protein. Altogether, our results suggested that the identified mutations in
300 *DNAH12* are probable pathogenic factors contributing to asthenoteratozoospermia in our patients.

301 **Impaired sperm motility and morphology in patients with bi-allelic *DNAH12* variants**

302 To assess the pathological effects of the identified bi-allelic *DNAH12* variants, semen analyses were
303 conducted following WHO guidelines (29). All affected individuals exhibited significantly reduced
304 sperm motility and progressive motility (Table 2). Detailed sperm morphology analyses were performed
305 on patients P3 from family 1, P5 from family 2, P8 from family 3, and three Chinese sporadic patients
306 (P9, P10, and P11). Spermatozoa from fertile controls displayed normal heads and tails, while
307 spermatozoa from the patients exhibited a range of abnormal morphologies, including short, coiled,
308 absent, bent, or irregular caliber flagella, accompanied by aberrant heads (Fig. 2A, Supplemental Figure
309 4, A and B). Scanning electron microscopy (SEM) analyses were further carried out on a fertile control
310 and P10, confirming the presence of abnormal morphologies of the sperm head and flagellum in the
311 patients (Fig. 2B). Thus, patients with the bi-allelic *DNAH12* variants demonstrated significantly
312 decreased sperm motility and increased abnormal sperm morphology.

313 **The bi-allelic *DNAH12* variants result in absence of DNAH12 protein in patients' sperm**

314 To investigate the effects of the identified bi-allelic *DNAH12* variants on the DNAH12 protein, we
315 obtained sperm samples from three affected Chinese patients, and the expression of DNAH12 was
316 detected using a custom-made DNAH12 rabbit antibody that recognized the N-terminal 1-200 amino
317 acids of the DNAH12 protein. This validated antibody (Supplemental Figure 6B) could theoretically

318 detect the truncated protein if it were present in P9 with a homozygous stop-gain mutation M4 (p.
319 Gln2077*). The predicted DNAH12 protein size was detected in the sperm lysate from a fertile control
320 but not in P9 with the homozygous stop-gain mutation M4, P10 with a homozygous missense mutation
321 M5, and P11 with compound heterozygous mutations M6 and M7, indicating these mutations possibly
322 lead to the disruption of the DNAH12 protein (Fig. 2C).

323 To further explore the effects of the identified *DNAH12* variants on the DNAH12 protein, we
324 performed immunofluorescence assays on sperm from patients. The results showed that DNAH12 signals
325 were localized along the flagella of the fertile control, however, no DNAH12 signals were observed in
326 sperm flagella of patients P3 (family 1), P5 (family 2), P8 (family 3), P9, P10, and P11 (Fig. 2D).
327 Collectively, these findings indicated that all the detected *DNAH12* variants cause the absence of
328 DNAH12 protein in the sperm of our patients, reinforcing that these *DNAH12* mutations are pathogenic
329 mutations of asthenoteratozoospermia in the patients.

330 **Patients with bi-allelic *DNAH12* variants exhibit flagellar axoneme defects**
331 Since patients with the bi-allelic *DNAH12* variants exhibited compromised sperm motility and abnormal
332 sperm morphology, we then investigated whether sperm flagellar ultrastructure was also affected in these
333 patients. TEM examination was performed on sperm flagella from both patients and normal fertile
334 controls. The flagella of fertile controls displayed the typical "9+2" microtubule structure with well-
335 organized DMTs and CP. In contrast, various defects were found in our patients, including loss of CP
336 (54.5%), disorganization of microtubules (26%), and absence of DMTs (16.5%) in the examined cross-
337 sections (Fig. 3A, 3C and Supplemental Figure 5A). To examine the IDAs impairment in axonemes, the
338 sections with intact ODAs were analyzed. Compared with axonemes in controls that almost all the
339 sections presented intact IDAs, approximately 70% of sections examined showed impaired IDA
340 structures in the analyzed three patients (Fig. 3B, 3D and Supplemental Figure 5A).

341 We then performed immunofluorescence assays on sperm smears to assess the expression and
342 localization of specific proteins of the axonemes. These included SPAG6 (a CP component), DNAH1
343 and DNALI1 (IDA components), DNAH17 (an ODA component), and ODF2 (an outer dense fiber, ODF
344 component). The sperm flagella of patients showed remarkably reduced SPAG6 signals when compared
345 with those from controls (Fig. 3E). Similarly, DNAH1 and DNALI1 signals were both obviously
346 decreased in the patients' sperm flagella, indicating impaired IDAs in the patients (Fig. 3F and G).
347 Besides, DNAH17 and ODF2 signals in patients' flagella were comparable to those in a normal control
348 (Fig. 3H and Supplemental Figure 5B). In summary, these findings indicated that the bi-allelic *DNAH12*
349 variants cause pronounced flagellar axoneme defects, including impaired IDAs and loss of CP, but do
350 not affect ODAs and ODFs.

351 **Deletion of *Dnah12* impairs spermiogenesis and causes male infertility in mice**
352 Considering the bi-allelic *DNAH12* variants resulting in absence of DNAH12 protein in patients' sperm,
353 to functionally confirm the deletion of *DNAH12*, we generated *Dnah12* knockout mice using CRISPR-
354 Cas9 approach (Supplemental Figure 6A). Fortunately, we obtained a mouse model with a 4-bp deletion
355 (c.386_389del) in exon 5 of *Dnah12* (Supplemental Figure 6A). In contrast to the observations in control
356 mice, immunoblotting of testis lysate using two antibodies targeting the N-terminal of DNAH12 failed
357 to detect DNAH12 proteins, and immunofluorescence staining of sperm flagella did not show DNAH12

358 signals in *Dnah12*$^{-/-}$ mice (Supplemental Figure 6, B and C). *Dnah12*$^{-/-}$ males exhibited normal
359 development but were infertile (Fig. 4A), while *Dnah12*$^{-/-}$ female mice showed normal development and
360 fertility, and no obvious defective oviductal and tracheal cilia (Supplemental Figure 7, A-C). The body
361 weight of *Dnah12*$^{-/-}$ and *Dnah12*$^{+/+}$ males was comparable, while smaller testes were observed in
362 *Dnah12*$^{-/-}$ males (Fig. 4B). Besides, the average number of sperm per epididymis of *Dnah12*$^{-/-}$ mice
363 dramatically decreased to approximately 2% of that of *Dnah12*$^{+/+}$ mice (Fig. 4C). The epididymal caudal
364 spermatozoa of *Dnah12*$^{-/-}$ male mice were 100% immotile, compared to those of *Dnah12*$^{+/+}$ mice (Fig.
365 4D, Supplemental Videos 1 and 2). H&E staining of testis and epididymis sections also showed a striking
366 reduction in the number of sperm in *Dnah12*$^{-/-}$ mice (Fig. 4E). Importantly, morphological analysis of
367 sperm from the caudal epididymis of *Dnah12*$^{-/-}$ mice showed similar types and frequencies of flagellum
368 and head abnormalities to those observed in our patients (Fig. 4F and G).

369 To understand how *DNAH12* depletion causes abnormal sperm morphology, we conducted
370 immunofluorescence assays on testicular cells from *Dnah12*$^{+/+}$ and *Dnah12*$^{-/-}$ mice, in *Dnah12*$^{-/-}$ mice,
371 while DNAH12 signals are missing in round, elongating, and elongated spermatids, the abnormal
372 manchette structure and flagellum were observed (Fig. 4H). We then performed immunofluorescence
373 assays on testicular sections using α-Tubulin and lectin peanut agglutinin (PNA, a marker of the
374 acrosome) to examine the process of spermiogenesis. The manchette structure in *Dnah12*$^{-/-}$ was roughly
375 normal until steps 9-10 (Stage IX-X) but was aberrantly stretched from steps 11-12 (Stage XI-XII) when
376 compared with those of *Dnah12*$^{+/+}$ mice (Supplemental Figure 8). To meticulously characterize these
377 defects, we stained α-Tubulin and PNA on squashed seminiferous tubules and found obvious manchette
378 defects and abnormal sperm heads in *Dnah12*$^{-/-}$ mice (Fig. 4I). TEM analysis showed severely abnormal
379 head morphology in elongated spermatids of *Dnah12*$^{-/-}$ males when compared with those of *Dnah12*$^{+/+}$
380 males (Fig. 4J). Additionally, TUNEL assays of testis sections showed dramatically increased
381 proportions of seminiferous tubules containing TUNEL-positive cells in *Dnah12*$^{-/-}$ mice, compared with
382 those in *Dnah12*$^{+/+}$ mice, suggesting the aberrant spermatids may undergo apoptosis (Figure 4K-M).
383 Altogether, these results indicated that deletion of *Dnah12* impairs spermiogenesis, results in decreased
384 sperm counts, and increased sperm morphological abnormalities in mice.

385 **Deletion of *Dnah12* causes axoneme defects in sperm flagella but not cilia in mice**

386 TEM analysis was conducted on sperm from cauda epididymis of *Dnah12*$^{+/+}$, *Dnah12*$^{+/-}$ and *Dnah12*$^{-/-}$
387 mice. Flagellar axonemes of *Dnah12*$^{+/+}$ and *Dnah12*$^{+/-}$ mice displayed a typical "9+2" microtubular
388 arrangement with clearly visible CP, IDAs, and ODAs. In contrast, sperm from *Dnah12*$^{-/-}$ mice exhibited
389 severe abnormalities in all the analyzed sections, characterized by CP loss and disorganized axoneme
390 structure (Fig. 5A). Immunoblotting was performed to assess the expression levels of DNAH1, DNALI1,
391 and SPAG6 in sperm lysates, *Dnah12*$^{-/-}$ sperm showed a significant reduction in the abundance of
392 DNAH1 and DNALI1, while the amount of DNAI2 (a component of ODAs) remained comparable to
393 *Dnah12*$^{+/+}$ and *Dnah12*$^{+/-}$ sperm (Fig. 5B). Additionally, immunofluorescence assays revealed the near
394 absence of signals for SPAG6, SPEF2 (a component of CP complex), DNAH1, and DNALI1 in *Dnah12*
395 $^{-/-}$ sperm flagella, whereas DNAH17 and DNAI2 (components of ODAs) remained unaffected (Fig. 5C-
396 H). These results indicate that DNAH12 deficiency specifically impairs CP and IDAs, but not ODAs, in
397 sperm flagella. Furthermore, immunoblotting of SPAG6 and DNALI1 in testis lysate exhibited a sharp
398 decrease in *Dnah12*$^{-/-}$ mice (Supplemental Figure 9A). Additionally, TEM examination of testicular
399 sperm axonemes showed defects like loss of CP and disarranged axonemes in *Dnah12*$^{-/-}$ mice

400 (Supplemental Figure 9B). These results indicate that impaired IDAs and loss of CP possibly occur
401 during testicular sperm flagellar development.

402 Another *Dnah12* mutant mouse model (*Dnah12*$^{mut/mut}$) targeting exon18 was also generated
403 (Supplemental Figure 10A), which may produce a truncated DNAH12 protein (p.Cys793Glu, fs*10).
404 The mutation effect was checked but no truncated DNAH12 protein was detected, indicating that
405 DNAH12 expression was disrupted in *Dnah12*$^{mut/mut}$ mice (Supplemental Figure 10B). Moreover,
406 *Dnah12*$^{mut/mut}$ mice developed normally, while decreased testicular size was observed (Supplemental
407 Figure 10, C and D). Consistent with *Dnah12*$^{-/-}$ mice and patients carrying bi-allelic *DNAH12* mutations,
408 *Dnah12*$^{mut/mut}$ presented obviously decreased sperm count, increased sperm morphological abnormalities,
409 and sperm axoneme defects similar to *Dnah12*$^{-/-}$ mice (Supplemental Figure 10, E-H). Therefore, these
410 results reconfirmed that DNAH12 is essential for sperm flagellar development.

411 Given the detection of DNAH12 protein in the trachea and lung (Supplemental Figure 2, A-C), we
412 also examined whether the deficiency of DNAH12 would cause PCD symptoms in males. Intriguingly,
413 both *Dnah12*$^{mut/mut}$ and *Dnah12*$^{-/-}$ males developed normally and showed no tracheal defects, despite the
414 expression of DNAH12 being detected in tracheal cilia cells (Supplemental Figure 11, A-E). These
415 findings collectively suggested that DNAH12 deficiency is crucial for sperm axonemal integrity in
416 humans and mice without manifesting PCD symptoms.

417 **DNAH12 interacts with IDA components DNAH1 and DNALI1**

418 Through phylogenetic and domain analyses of DNAH family members, we found that DNAH12 is a
419 distinctive IDA lacking the microtubule-binding domain (MTBD), which is crucial for ATP-sensitive
420 microtubule binding and motor direction control (Fig.6A, Supplemental Figure 12). Therefore, DNAH12
421 likely collaborates with other members to carry out its functions. To delve into the molecular mechanism
422 of DNAH12, we conducted co-immunoprecipitation (Co-IP) followed by mass spectrometry analysis
423 using a DNAH12 rabbit antibody in testicular lysate from adult *Dnah12*$^{+/+}$ mice (Fig. 6B). Gene ontology
424 analysis showed that the potential interactors were mainly enriched in motor protein, actin binding,
425 myosin and RNA binding proteins (Fig. 6C). The motor proteins were predominantly categorized into
426 three groups: dynein, kinesin, and myosin protein members, interestingly, among these, dynein proteins
427 such as DNAH1, DNALI1, DNAH1, DNAH3, and DNAH2 were annotated to be involved in IDA
428 assembly, which is closely related to the defects found in *DNAH12* mutants (Fig. 6D). This piqued our
429 interest to explore these proteins in detail. Besides the predominant enrichment of DNAH12 (top1),
430 potential IDA interactors such as DNALI1 (top2), DNAH1 (top3), DNAH3 (top4), and DNAH2 (top5)
431 were co-enriched in the candidate interacting dynein protein list (Supplemental Table 5). Immunoblotting
432 confirmed the co-enrichment of DNAH12, DNALI1, and DNAH1 in the immunoprecipitated complex
433 by the DNAH12 rabbit antibody in *Dnah12*$^{+/+}$ mice but not in *Dnah12*$^{-/-}$ mice, indicating specific
434 interactions between DNAH12 and DNALI1, DNAH1 (Fig. 6E). Reciprocal in vivo Co-IP using an anti-
435 DNALI1 antibody further validated strong interactions among these three IDA components (Fig. 6F).

436 Given the potential role of DNALI1 as an IDA assembly factor (47), we delved into the interaction
437 details between DNAH12 and DNALI1. Employing Phyre2, we constructed the structural models of both
438 proteins and further elucidated their interaction dynamics via DNAH12-DNALI1 docking using the
439 HDOCK server. The results showed that the N-terminal Stem domain of DNAH12 possibly interacts

440 with DNALI1 in the top three best-fit conformations (Fig. 6G). Considering DNAH12 is encoded by
441 3092 amino acids and their full-length protein interactions have been proved in vivo, we constructed the
442 Stem domain (1-1212 amino acids) of DNAH12 and full-length DNALI1 plasmid, further in vitro Co-IP
443 assays validated that the Stem domain of DNAH12 indeed mediates interactions with DNALI1 (Fig. 6H-
444 J). Together, these findings proved the specific interactions among DNAH12, DNALI1, and DNAH1.
445 Given the significantly decreased protein levels of DNALI1 and DNAH1 observed in the sperm of
446 *Dnah12*$^{-/-}$mice (Fig.5B), we proposed that the interactions involving DNAH12 (possibly restricted to the
447 Stem domain of DNAH12), DNALI1, and DNAH1 are crucial for flagella development. As dynein
448 proteins typically share similar domains, our findings also suggested that the Stem domain of DNAH
449 family members may facilitate the interaction with DNALI1.

450 **Deletion of DNAH12 impairs the recruitment of IDA components during flagella development**
451 To evaluate the effect of DNAH12 deletion on DNALI1 and DNAH1 during spermiogenesis, we
452 examined the abundance of the DNAH12 interaction partners, DNALI1 and DNAH1, in *Dnah12*$^{+/+}$ and
453 *Dnah12*$^{-/-}$ mouse testis lysate. The protein levels of DNALI1 and DNAH1 were decreased in *Dnah12*$^{-/-}$
454 testes, while the level of ODA member DNAI1 was comparable (Fig. 7A). We then stained DNALI1 or
455 DNAH1 on testicular cell smear of *Dnah12*$^{+/+}$ and *Dnah12*$^{-/-}$ mice. Although the signals of DNALI1 or
456 DNAH1 in round spermatids of *Dnah12*$^{-/-}$ mice were comparable to those of *Dnah12*$^{+/+}$ mice (Fig. 7B
457 and 7C), the recruitment of DNALI1 and DNAH1 to sperm flagella was severely impaired in elongated
458 spermatids of *Dnah12*$^{-/-}$ mice (Fig.7D and 7E). Considering that the deficiency of DNAH12 also caused
459 scarcely visible immunofluorescence signals of DNALI1 and DNAH1 in sperm flagella of humans and
460 mice (Fig. 3F, 3G, 5E, and 5F), we proposed that the interaction among DNAH12, DNALI1, and DNAH1
461 is conserved in mammals, and is required for flagellar development during spermiogenesis. Since the
462 deficiency of DNAH12 does not cause PCD symptoms in humans and mice, we hypothesized that
463 flagella and cilia may exhibit distinct features in the process of dynein assembly. We thus checked the
464 abundance of DNALI1 and DNAH1 in the oviduct and trachea, the results showed that DNALI1 and
465 DNAH1 were comparable in the *Dnah12*$^{+/+}$ and *Dnah12*$^{-/-}$ groups (Fig. 7F and 7G). Furthermore, no
466 discernible disparities were observed in the intensity and localization of DNALI1 and DNAH1 signals
467 within the oviduct and trachea (Fig. 7H-K). In summary, these results underscore the specific
468 involvement of DNAH12 in flagellar development, rather than in cilial development. Moreover, we
469 supposed that the assembly of IDA components differs between flagella and cilia.

470 **DNAH12 is prerequisite for the recruitment of DNALI1 and DNAH1 to sperm flagella**
471 In patients and mice with DNALI1 deficiency, flagellar DNAH1 but not DNAH12 signals were absent
472 (47). To unravel the recruitment relationships among DNAH12, DNALI1, and DNAH1 during sperm
473 flagellar formation, we conducted staining of DNALI1 and DNAH12 on sperm flagella obtained from
474 the infertile asthenoteratozoospermic male P13 with a homozygous *DNAH1* mutation (c.11275C>T) of
475 a family (Fig. 7L, and Supplemental Figure13 A and B), wherein DNAH1 signals were absent along the
476 flagella (Fig. 7M). In comparison to those in the control, the DNALI1 signals were absent, while no
477 discernible differences in DNAH12 signals were observed in the flagella of the patient with the *DNAH1*
478 mutation (Fig. 7N and 7O). These findings suggested that the recruitment of DNAH12 to flagella is
479 independent of DNAH1, and DNAH12 is the first protein to be recruited to flagella among the three
480 proteins.

481 **DNAH12 deficiency causes the decrease of RS head associated proteins**

482 In addition to the enrichment of dynein proteins, we noticed that a clusters of RS head-related proteins
483 such as RSPH1, RSPH9, or DNAJB13 were enriched in the testicular interactome of DNAH12.
484 Considering that deficiency in RSPH1 (48), RSPH9 (49), or DNAJB13 (50) were associated with CP
485 loss phenotype. We then explored their interaction with DNAH12 in the testis lysate, the results proved
486 the interactions of these proteins with DNAH12 in the testis (Fig. 8A). Further analyses by AlphaFold3
487 showed that these proteins may interacts with DNAH12 through Stem domain (Fig. 8B). The expression
488 of RSPH1, RSPH9, and DNAJB13 showed obvious decrease in testis lysate of *Dnah12*$^{-/-}$ mice (Fig. 8C).
489 Additionally, immunofluorescence assays revealed the loss of signals for RSPH1, a marker of RS head,
490 in *Dnah12*$^{-/-}$ sperm flagella (Fig. 8D). Together, these results indicate that deficiency of DNAH12 lead
491 to the impairment of radial spoke head, which could contribute to CP loss in flagella of *Dnah12*$^{-/-}$ mice.

492 **ICSI may overcome the infertility caused by DNAH12 deficiency**

493 Since the DNAH12 mutated patients and the *Dnah12*$^{-/-}$ mice have similar deficiency, to evaluate the
494 prospects of whether the asthenoteratozoospermia patients caused by *DNAH12* variants could be treated
495 with assisted reproductive technology, spermatozoa from D*nah12*$^{+/+}$ and *Dnah12*$^{-/-}$ mice were used for
496 ICSI. Promisingly, the percentages of 2-cell and blastocyst-stage embryos in *Dnah12*$^{-/-}$ group showed
497 no difference compared to those of *Dnah12*$^{+/+}$ group (Fig. 8E-G), indicating that ICSI could also be an
498 effective treatment for infertile men carrying *DNAH12* variants.

499 Taken together, we suggest that DNAH12 interacts with DNALI1 and DNAH1, and this interaction
500 is a prerequisite for the proper localization of DNALI1 and DNAH1 to sperm flagella, which is essential
501 for the intact IDAs and CP structures in both humans and mice. Additionally, DNALI1 and DNAH1
502 exhibit mutual dependence for their localization to sperm flagella. Deficiency of DNAH12 leads to the
503 failure of DNALI1 and DNAH1 recruitment to sperm flagella, resulting in abnormal sperm morphology
504 characterized by compromised axoneme organization, causing male infertility (Fig. 8H). Moreover, our
505 results indicate that the assembly of IDA components occurs intricately, possibly not synchronously in
506 time and space.

507 **Discussion**

508 In this study, we identified six novel bi-allelic mutations in *DNAH12* that cause the loss of DNAH12
509 proteins in asthenoteratozoospermia patients. Spermatozoa from these patients exhibited abnormal
510 morphology and compromised axonemal defects, including a high percentage of impaired IDAs and loss
511 of CP. Two mouse models (*Dnah12*$^{-/-}$ *and Dnah12*$^{mut/mut}$) were generated, recapitulating the abnormal
512 flagellum morphology and structure observed in patients, thereby confirming the pathogenic role of
513 *DNAH12* mutations in asthenoteratozoospermia. Through testicular Co-IP and mass spectrometry
514 proteomics, we screened and validated that DNAH12 interacts with IDA components like DNALI1 and
515 DNAH1 and is indispensable for recruiting DNALI1 and DNAH1 to sperm flagella, highlighting the
516 crucial role of DNAH12 in sperm flagellar development. Notably, deficiency of DNAH12 does not
517 manifest PCD symptoms in humans and mice, underscoring the unique role of DNAH12 in flagellar
518 development. Collectively, our study not only unveils the functional significance of the previously
519 unexplored gene *DNAH12* but also elucidates the pathogenic link between *DNAH12* mutations and
520 asthenoteratozoospermia.

521 DNAH12 and other dynein arm proteins share the N-terminal Stem domain, which is crucial for
522 structure and accessory subunit binding (51), and the motor domain which encompasses ~6 AAA+
523 ATPase modules forming the ring-shaped oligomeric complexes responsible for force production (52).
524 Five of the identified *DNAH12* mutations, primarily in the Stem domain (critical for DNALI1 interaction),
525 result in loss-of-function effects, indicating a weak tolerance property of the Stem domain. Similar weak
526 tolerance features were observed in mutations of other dynein arm components like *DNAH1* and *DNAH2*
527 (53, 54). The profound impact of these variants, particularly missense mutations, underscores delicate
528 features of the Stem domain and DNAH family members. Notably, DNAH12 stands out as the shortest
529 in sequence length and the only one lacking the essential MTBD domain within the DNAH family (55).
530 MTBD, a 15-nanometer coiled-coil stalk structure, crucially supports ATP-sensitive microtubule binding
531 properties and determines dynein motility direction (56). Our investigation revealed that DNAH12
532 interacts with other IDA components, specifically DNALI1 and DNAH1. Despite the mutual dependence
533 between DNAH1 and DNALI1 for their flagellar localization, DNAH12 is prerequisite for the proper
534 assembly of DNALI1 and DNAH1 onto sperm flagella in both humans and mice. Notably, *Dnah12*$^{-/-}$
535 mice exhibit more severe phenotypes than *Dnali1* and *Dnah1* knockout mice (4, 47, 57), including a
536 more severe reduced sperm count (~ 2% of normal values), this observation further supports our
537 perspective.

538 Deficiency in DNAH12 presented sperm ultrastructural defects like CP loss and impaired IDAs
539 indicating essential roles of DNAH12 in the maintenance of axonemal integrity and arrangement. These
540 results indicate essential roles of DNAH12 in the maintenance of axonemal integrity and arrangement.
541 Noteworthy, deficiency of DNAH12 potential partner DNAH1, a well-known asthenoteratozoospermia-
542 related gene, presents quite similar defects with DNAH12, indicating DNAH12 and DNAH1 possibly
543 exhibit synergic functions in axonemal proper arrangement (58-60). In addition to DNAH12 and DNAH1,
544 deficiency in DNAH2 or DNAH6 also leads to high proportions of CP loss and disorganized axonemal
545 structures (5, 54, 61). However, DNALI1, DNAH7, or DNAH10 deficiency results in no obvious CP loss
546 but impaired IDA integrity (7, 8, 22, 47). These studies indicate that specific IDA components, like
547 DNAH12 and DNAH1, are required for the maintenance of CP integrity. Moreover, discrepancies
548 observed in the phenotypes resulting from deficiencies in specific IDAs suggest that multiple dynein
549 proteins are produced to support the intricate organization of sperm flagella. Additionally, these proteins
550 may exhibit distinct characteristics and perform unique functions to some extent. Noteworthy, deficiency
551 in RS head proteins RSPH1, RSPH9, or DNAJB13 were related to axonemal CP loss phenotype (48, 50,
552 62), indicating that DNAH12, and other IDAs, possibly regulate the stability of CP through the
553 cooperation with RS head proteins.

554 The localization of DNAH12 presents dynamic changes during spermiogenesis. DNAH12 is
555 initially expressed in the cytoplasm of the round spermatid, while it's enriched in the manchette structure
556 of the elongating spermatid and the tail of the elongated spermatid. The manchette and the sperm tail
557 axoneme are two microtubular platforms that transport proteins to the developing head and tail (63).
558 Manchette is a transient skirt-like structure and functions as a scaffold for morphological remodeling,
559 contributing to the formation of the sperm head, neck, and tail (64). Here, we found that DNAH12
560 deficiency results in abnormal manchette structure and compromised sperm head and tail morphology.
561 Additionally, in sperm of *Dnah12*$^{-/-}$ males, several CP complex proteins like SPAG6, and SPEF2 are not
562 properly assembled and the axoneme structure of the tail was severely disorganized, indicating dynein

563 components are responsible for proper axonemal components organization. Noteworthy, DNALI1, a
564 potential DNAH12 interacting partner showed similar localization patterns to DNAH12, a study
565 presented that DNALI1 recruits and stabilizes manchette component PACRG, and DNALI1 deficiency
566 causes impaired sperm flagellar assembly (57). These data hint that dynein proteins like DNAH12 and
567 DNALI, possibly work together in the manchette organization as well as sperm flagellar components
568 assembly during sperm development.

569 DNAH12 was also detected in the lungs, tracheas, and female oviducts while no cilia morphology
570 defects in these tissues or PCD symptoms were observed in both two mice models. Besides, none of the
571 patients carrying bi-allelic *DNAH12* mutations claimed symptoms of PCD via visits except for the
572 reproductive problems. *Dnah12*$^{-/-}$ female mice showed normal development and fertility and the mother
573 (III:2) of patients from family 2, carrying homozygous *DNAH12* mutation M2 had 6 offspring.
574 Intriguingly, we found that the localization and abundance of DNALI1 and DNAH1 in oviductal or
575 tracheal cilia were not affected after *Dnah12* deletion, indicating that DNAH12 works differently in
576 flagella and cilia. Deficiency of specific DNAH members like DNAH6 (65), or DNAH7 (22), but not
577 DNAH2 (54), results in PCD symptoms. Hence, DNAH family members possibly present disparate
578 processing of axonemal biogenesis and organization through evolution in flagella and cilia, further
579 explorations could contribute to a more comprehensive understanding of the differences between flagella
580 and cilia, and personalized clinical diagnosis of related diseases like male/female infertility and/or PCD
581 (66).

582 Previously, two genetic screening studies mentioned unverified compound heterozygous mutations
583 and a homozygous missense mutation in *DNAH12*, predicting their association with patients' infertility.
584 However, limited genetic evidence was provided, and the pathogenesis remained unclear (26, 27).
585 Through investigations involving patients with *DNAH12* variants and mutant mouse models, we provide
586 direct genetic and molecular evidence that variants in *DNAH12* are genetic causes of
587 asthenoteratozoospermia, and DNAH12 along with DNAH1, DNALI1 is indispensable for sperm
588 flagellar biogenesis. These data strongly support DNAH12 as a valuable marker in genetic counseling
589 and diagnosis of male infertility.

590 ICSI is a widely used assisted reproductive technology in treating infertile men with
591 asthenoteratozoospermia. Deficiency in most dynein proteins leads to asthenoteratozoospermia with
592 severely compromised sperm motility and morphology. Previous studies have shown that patients
593 carrying mutations in *DNAH17* (10) have poor ICSI outcomes while patients with *DNAH1*(59), *DNAH2*
594 (5, 61), *DNAH3* (67), *DNAH7* (22), or *DNAH8* (68) mutations have achieved favorable clinical pregnancy.
595 Thus, the comparative study of asthenoteratozoospermia-related genes on their ICSI outcomes will be
596 beneficial to developing individualized treatment recommendations in clinical practice. In our study, the
597 successful ICSI outcomes of *Dnah12*$^{-/-}$ mice suggest that ICSI could be used as a potential treatment for
598 infertile men carrying *Dnah12* mutations. It's meaningful to evaluate the prognosis for ICSI treatments
599 in patients carrying *DNAH12* variants in a large population.

600 In conclusion, our study functionally and mechanistically sheds light on a special and poorly
601 characterized protein DNAH12, during the intricate process of sperm flagellar biogenesis. These results
602 pave the way for an enhanced understanding of the roles of dynein proteins in sperm flagellar

development and their functional difference in flagella and cilia, offering a diagnostic target for genetic counseling and future individualized treatment of male infertility in clinical practice.

Data availability

All data that support the findings in this study are available from the corresponding author upon reasonable request. Proteomics data supporting this study have been deposited to the ProteomeXchange Consortium via the iProX partner repository with the dataset identifier PXD051681.

Author contributions

B.S. and Q.S. conceived and supervised the study; M.Y., X.H., J.Y, M.C., A.Z., T.L., A.Z., and N.A. performed the experiments and analyzed the data; H.M.J, M.K., Z.M., R.K., A.A., and W.S. collected the patients' samples; J.Z. and H.Z. performed the WES sequencing and data analyses; M.Y. wrote the manuscript and B.S., Q.S., H.M., and M.Y. modified the manuscript; B.S., Q.S, H.M., B.X., H.Z., and A.M. were involved in discussions of the manuscript.

Ethics statement

This work was approved by the institutional ethics committee of University of Science and Technology of China (USTC) with the approval number 2019-KY-168, and informed consent was obtained from patients and controls. All animal experiments were approved by the Institutional Animal Care and Use Committee of the USTC with the approval number USTCACUC1301021.

Funding

This work was supported by the National Key Research and Development Program of China (2022YFC2702601, 2022YFA0806303, and 2019YFA0802600), the National Natural Science Foundation of China (82171599, 32270901, and 32070850), the Global Select Project (DJK-LX-2022010) of the Institute of Health and Medicine, Hefei Comprehensive National Science Center, the Joint Fund for New Medicine of USTC (YD9100002034) and Scientific Research Foundation for Scholars of the First Affiliated Hospital of USTC (RC2023054).

Declaration of competing interest

The authors declare that they have no known competing financial interests or personal relationships that could have appeared to influence the work reported in this paper.

Acknowledgments

We are grateful to all the participants for their cooperation. We appreciated Li Wang and Dandan Song at the Center of Cryo-Electron Microscopy, Zhejiang University, for their technical assistance with TEM and SEM, respectively. We thank the Bioinformatics Center of the USTC, School of Life Sciences, for providing supercomputing resources.

References

1. Agarwal A, Baskaran S, Parekh N, Cho C-L, Henkel R, Vij S, et al. Male infertility. *Lancet.* 2021;397(10271):319-33.
2. Krausz C, and Riera-Escamilla A. Genetics of male infertility. *Nat Rev Urol.* 2018;15(6):369-84.

647 3. Shang X, Shen C, Liu J, Tang L, Zhang H, Wang Y, et al. Serine protease PRSS55 is crucial for
648 male mouse fertility via affecting sperm migration and sperm-egg binding. *Cell Mol Life Sci.*
649 2018;75(23):4371-84.
650 4. Khan R, Zaman Q, Chen J, Khan M, Ma A, Zhou J, et al. Novel Loss-of-Function Mutations in
651 DNAH1 Displayed Different Phenotypic Spectrum in Humans and Mice. *Front Endocrinol*
652 *(Lausanne).* 2021;12:765639.
653 5. Li Y, Sha Y, Wang X, Ding L, Liu W, Ji Z, et al. DNAH2 is a novel candidate gene associated
654 with multiple morphological abnormalities of the sperm flagella. *Clin Genet.* 2019;95(5):590-
655 600.
656 6. Tu C, Nie H, Meng L, Yuan S, He W, Luo A, et al. Identification of DNAH6 mutations in
657 infertile men with multiple morphological abnormalities of the sperm flagella. *Sci Rep.*
658 2019;9(1):15864.
659 7. Gao Y, Liu L, Shen Q, Fu F, Xu C, Geng H, et al. Loss of function mutation in DNAH7 induces
660 male infertility associated with abnormalities of the sperm flagella and mitochondria in human.
661 *Clinical Genetics.* 2022;102(2):130-5.
662 8. Li K, Wang G, Lv M, Wang J, Gao Y, Tang F, et al. Bi-allelic variants in DNAH10 cause
663 asthenoteratozoospermia and male infertility. *J Assist Reprod Genet.* 2022;39(1):251-9.
664 9. Liu C, Miyata H, Gao Y, Sha Y, Tang S, Xu Z, et al. Bi-allelic DNAH8 Variants Lead to Multiple
665 Morphological Abnormalities of the Sperm Flagella and Primary Male Infertility. *Am J Hum*
666 *Genet.* 2020;107(2):330-41.
667 10. Whitfield M, Thomas L, Bequignon E, Schmitt A, Stouvenel L, Montantin G, et al. Mutations
668 in DNAH17, Encoding a Sperm-Specific Axonemal Outer Dynein Arm Heavy Chain, Cause
669 Isolated Male Infertility Due to Asthenozoospermia. *Am J Hum Genet.* 2019;105(1):198-212.
670 11. Zhang B, Ma H, Khan T, Ma A, Li T, Zhang H, et al. A DNAH17 missense variant causes
671 flagella destabilization and asthenozoospermia. *J Exp Med.* 2020;217(2).
672 12. Coutton C, Vargas AS, Amiri-Yekta A, Kherraf ZE, Ben Mustapha SF, Le Tanno P, et al.
673 Mutations in CFAP43 and CFAP44 cause male infertility and flagellum defects in Trypanosoma
674 and human. *Nat Commun.* 2018;9(1):686.
675 13. Tang S, Wang X, Li W, Yang X, Li Z, Liu W, et al. Biallelic Mutations in CFAP43 and CFAP44
676 Cause Male Infertility with Multiple Morphological Abnormalities of the Sperm Flagella. *Am J*
677 *Hum Genet.* 2017;100(6):854-64.
678 14. Ma A, Zhou J, Ali H, Abbas T, Ali I, Muhammad Z, et al. Loss-of-function mutations in CFAP57
679 cause multiple morphological abnormalities of the flagella in humans and mice. *JCI Insight.*
680 2023;8(3).
681 15. Hu T, Meng L, Tan C, Luo C, He WB, Tu C, et al. Biallelic CFAP61 variants cause male
682 infertility in humans and mice with severe oligoasthenoteratozoospermia. *J Med Genet.*
683 2023;60(2):144-53.
684 16. Toure A, Martinez G, Kherraf ZE, Cazin C, Beurois J, Arnoult C, et al. The genetic architecture
685 of morphological abnormalities of the sperm tail. *Hum Genet.* 2021;140(1):21-42.
686 17. Walton T, Gui M, Velkova S, Fassad MR, Hirst RA, Haarman E, et al. Axonemal structures
687 reveal mechanoregulatory and disease mechanisms. *Nature.* 2023;618(7965):625-33.
688 18. Viswanadha R, Sale WS, and Porter ME. Ciliary Motility: Regulation of Axonemal Dynein
689 Motors. *Cold Spring Harb Perspect Biol.* 2017;9(8).
690 19. Kleinboelting S, Diaz A, Moniot S, van den Heuvel J, Weyand M, Levin LR, et al. Crystal

691 structures of human soluble adenylyl cyclase reveal mechanisms of catalysis and of its
692 activation through bicarbonate. *Proc Natl Acad Sci U S A.* 2014;111(10):3727-32.
693 20. Shoemark A, Burgoyne T, Kwan R, Dixon M, Patel MP, Rogers AV, et al. Primary ciliary
694 dyskinesia with normal ultrastructure: three-dimensional tomography detects absence of
695 DNAH11. *Eur Respir J.* 2018;51(2).
696 21. Sironen A, Shoemark A, Patel M, Loebinger MR, and Mitchison HM. Sperm defects in primary
697 ciliary dyskinesia and related causes of male infertility. *Cell Mol Life Sci.* 2020;77(11):2029-48.
698 22. Wei X, Sha Y, Wei Z, Zhu X, He F, Zhang X, et al. Bi-allelic mutations in DNAH7 cause
699 asthenozoospermia by impairing the integrality of axoneme structure. *Acta Biochim Biophys*
700 *Sin (Shanghai).* 2021;53(10):1300-9.
701 23. Gao Y, Liu L, Shen Q, Fu F, Xu C, Geng H, et al. Loss of function mutation in DNAH7 induces
702 male infertility associated with abnormalities of the sperm flagella and mitochondria in human.
703 *Clin Genet.* 2022;102(2):130-5.
704 24. Imtiaz F, Allam R, Ramzan K, and Al-Sayed M. Variation in DNAH1 may contribute to primary
705 ciliary dyskinesia. *BMC Med Genet.* 2015;16:14.
706 25. Vaisberg EA, Grissom PM, and McIntosh JR. Mammalian cells express three distinct dynein
707 heavy chains that are localized to different cytoplasmic organelles. *J Cell Biol.*
708 1996;133(4):831-42.
709 26. Li Y, Wang Y, Wen Y, Zhang T, Wang X, Jiang C, et al. Whole-exome sequencing of a cohort of
710 infertile men reveals novel causative genes in teratozoospermia that are chiefly related to sperm
711 head defects. *Hum Reprod.* 2021.
712 27. Oud MS, Houston BJ, Volozonoka L, Mastrorosa FK, Holt GS, Alobaidi BKS, et al. Exome
713 sequencing reveals variants in known and novel candidate genes for severe sperm motility
714 disorders. *Hum Reprod.* 2021;36(9):2597-611.
715 28. Chapelin C, Duriez B, Magnino F, Goossens M, Escudier E, and Amselem S. Isolation of several
716 human axonemal dynein heavy chain genes: genomic structure of the catalytic site, phylogenetic
717 analysis and chromosomal assignment. *FEBS Lett.* 1997;412(2):325-30.
718 29. World Health Organization. *WHO Laboratory Manual for the Examination and Processing of*
719 *Human Semen.*: 6th edn. Geneva： World Health Organization; 2021.
720 30. Wang K, Li M, and Hakonarson H. ANNOVAR: functional annotation of genetic variants from
721 high-throughput sequencing data. *Nucleic Acids Res.* 2010;38(16):e164.
722 31. Yin H, Ma H, Hussain S, Zhang H, Xie X, Jiang L, et al. A homozygous FANCM frameshift
723 pathogenic variant causes male infertility. *Genet Med.* 2019;21(1):62-70.
724 32. Narasimhan V, Danecek P, Scally A, Xue Y, Tyler-Smith C, and Durbin R. BCFtools/RoH: a
725 hidden Markov model approach for detecting autozygosity from next-generation sequencing
726 data. *Bioinformatics.* 2016;32(11):1749-51.
727 33. Tamura K, Stecher G, and Kumar S. MEGA11: Molecular Evolutionary Genetics Analysis
728 Version 11. *Mol Biol Evol.* 2021;38(7):3022-7.
729 34. He Z, Zhang H, Gao S, Lercher MJ, Chen WH, and Hu S. Evolview v2: an online visualization
730 and management tool for customized and annotated phylogenetic trees. *Nucleic Acids Res.*
731 2016;44(W1):W236-41.
732 35. Chen C, Chen H, Zhang Y, Thomas HR, Frank MH, He Y, et al. TBtools: An Integrative Toolkit
733 Developed for Interactive Analyses of Big Biological Data. *Mol Plant.* 2020;13(8):1194-202.
734 36. Mistry J, Chuguransky S, Williams L, Qureshi M, Salazar GA, Sonnhammer ELL, et al. Pfam:

735 The protein families database in 2021. *Nucleic Acids Res.* 2021;49(D1):D412-D9.
736 37. Kelley LA, Mezulis S, Yates CM, Wass MN, and Sternberg MJ. The Phyre2 web portal for
737 protein modeling, prediction and analysis. *Nat Protoc.* 2015;10(6):845-58.
738 38. Pettersen EF, Goddard TD, Huang CC, Couch GS, Greenblatt DM, Meng EC, et al. UCSF
739 Chimera--a visualization system for exploratory research and analysis. *J Comput Chem.*
740 2004;25(13):1605-12.
741 39. Ma H, Zhang B, Khan A, Zhao D, Ma A, Zhou J, et al. Novel frameshift mutation in STK33 is
742 associated with asthenozoospermia and multiple morphological abnormalities of the flagella.
743 *Hum Mol Genet.* 2021;30(21):1977-84.
744 40. Ma H, Li T, Xie X, Jiang L, Ye J, Gong C, et al. RAD51AP2 is required for efficient meiotic
745 recombination between X and Y chromosomes. *Sci Adv.* 2022;8(2):eabk1789.
746 41. Zhang B, Khan I, Liu C, Ma A, Khan A, Zhang Y, et al. Novel loss-of-function variants in
747 DNAH17 cause multiple morphological abnormalities of the sperm flagella in humans and mice.
748 *Clin Genet.* 2021;99(1):176-86.
749 42. Dil S, Khan A, Unar A, Yang ML, Ali I, Zeb A, et al. A novel homozygous frameshift variant in
750 DNAH8 causes multiple morphological abnormalities of the sperm flagella in a consanguineous
751 Pakistani family. *Asian J Androl.* 2022.
752 43. Wang H, Yang H, Shivalila CS, Dawlaty MM, Cheng AW, Zhang F, et al. One-step generation
753 of mice carrying mutations in multiple genes by CRISPR/Cas-mediated genome engineering.
754 *Cell.* 2013;153(4):910-8.
755 44. Xu J, Gao J, Liu J, Huang X, Zhang H, Ma A, et al. ZFP541 maintains the repression of pre-
756 pachytene transcriptional programs and promotes male meiosis progression. *Cell Rep.*
757 2022;38(12):110540.
758 45. Chen T, Ma J, Liu Y, Chen Z, Xiao N, Lu Y, et al. iProX in 2021: connecting proteomics data
759 sharing with big data. *Nucleic Acids Res.* 2022;50(D1):D1522-d7.
760 46. Gao J, Zhang H, Jiang X, Ali A, Zhao D, Bao J, et al. FertilityOnline: A Straightforward Pipeline
761 for Functional Gene Annotation and Disease Mutation Discovery. *Genomics Proteomics*
762 *Bioinformatics.* 2022;20(3):455-65.
763 47. Wu H, Liu Y, Li Y, Li K, Xu C, Gao Y, et al. DNALI1 deficiency causes male infertility with
764 severe asthenozoospermia in humans and mice by disrupting the assembly of the flagellar inner
765 dynein arms and fibrous sheath. *Cell Death Dis.* 2023;14(2):127.
766 48. Lin J, Yin W, Smith MC, Song K, Leigh MW, Zariwala MA, et al. Cryo-electron tomography
767 reveals ciliary defects underlying human RSPH1 primary ciliary dyskinesia. *Nat Commun.*
768 2014;5:5727.
769 49. Zhu L, Liu H, Chen Y, Yan X, and Zhu X. Rsph9 is critical for ciliary radial spoke assembly
770 and central pair microtubule stability. *Biol Cell.* 2019;111(2):29-38.
771 50. Liu M, Li J, Jiang C, Zhou Y, Sun Y, Yang Y, et al. A novel homozygous mutation in DNAJB13-
772 a gene associated with the sperm axoneme-leads to teratozoospermia. *J Assist Reprod Genet.*
773 2022;39(3):757-64.
774 51. Kollmar M. Fine-Tuning Motile Cilia and Flagella: Evolution of the Dynein Motor Proteins
775 from Plants to Humans at High Resolution. *Mol Biol Evol.* 2016;33(12):3249-67.
776 52. Canty JT, Tan R, Kusakci E, Fernandes J, and Yildiz A. Structure and Mechanics of Dynein
777 Motors. *Annu Rev Biophys.* 2021;50:549-74.
778 53. Sha Y, Yang X, Mei L, Ji Z, Wang X, Ding L, et al. DNAH1 gene mutations and their potential

779 association with dysplasia of the sperm fibrous sheath and infertility in the Han Chinese
780 population. *Fertil Steril.* 2017;107(6):1312-8 e2.
781 54. Hwang JY, Nawaz S, Choi J, Wang H, Hussain S, Nawaz M, et al. Genetic Defects in DNAH2
782 Underlie Male Infertility With Multiple Morphological Abnormalities of the Sperm Flagella in
783 Humans and Mice. *Front Cell Dev Biol.* 2021;9:662903.
784 55. Lacey SE, He S, Scheres SH, and Carter AP. Cryo-EM of dynein microtubule-binding domains
785 shows how an axonemal dynein distorts the microtubule. *Elife.* 2019;8.
786 56. Carter AP, Garbarino JE, Wilson-Kubalek EM, Shipley WE, Cho C, Milligan RA, et al.
787 Structure and functional role of dynein's microtubule-binding domain. *Science.*
788 2008;322(5908):1691-5.
789 57. Yap YT, Li W, Huang Q, Zhou Q, Zhang D, Sheng Y, et al. DNALI1 interacts with the
790 MEIG1/PACRG complex within the manchette and is required for proper sperm flagellum
791 assembly in mice. *Elife.* 2023;12.
792 58. Ben Khelifa M, Coutton C, Zouari R, Karaouzene T, Rendu J, Bidart M, et al. Mutations in
793 DNAH1, which encodes an inner arm heavy chain dynein, lead to male infertility from multiple
794 morphological abnormalities of the sperm flagella. *Am J Hum Genet.* 2014;94(1):95-104.
795 59. Wambergue C, Zouari R, Fourati Ben Mustapha S, Martinez G, Devillard F, Hennebicq S, et al.
796 Patients with multiple morphological abnormalities of the sperm flagella due to DNAH1
797 mutations have a good prognosis following intracytoplasmic sperm injection. *Hum Reprod.*
798 2016;31(6):1164-72.
799 60. Wang M, Yang QY, Zhou JP, Tan HP, Hu J, Jin L, et al. Novel compound heterozygous mutations
800 in DNAH1 cause primary infertility in Han Chinese males with multiple morphological
801 abnormalities of the sperm flagella. *Asian J Androl.* 2022.
802 61. Gao Y, Tian S, Sha Y, Zha X, Cheng H, Wang A, et al. Novel bi-allelic variants in DNAH2 cause
803 severe asthenoteratozoospermia with multiple morphological abnormalities of the flagella.
804 *Reprod Biomed Online.* 2021;42(5):963-72.
805 62. Zou W, Lv Y, Liu ZI, Xia P, Li H, and Jiao J. Loss of Rsph9 causes neonatal hydrocephalus with
806 abnormal development of motile cilia in mice. *Sci Rep.* 2020;10(1):12435.
807 63. Lehti MS, and Sironen A. Formation and function of the manchette and flagellum during
808 spermatogenesis. *Reproduction.* 2016;151(4):R43-54.
809 64. Hu W, Zhang R, Xu H, Li Y, Yang X, Zhou Z, et al. CAMSAP1 role in orchestrating structure
810 and dynamics of manchette microtubule minus-ends impacts male fertility during
811 spermiogenesis. *Proc Natl Acad Sci U S A.* 2023;120(45):e2313787120.
812 65. Li Y, Yagi H, Onuoha EO, Damerla RR, Francis R, Furutani Y, et al. DNAH6 and Its Interactions
813 with PCD Genes in Heterotaxy and Primary Ciliary Dyskinesia. *PLoS Genet.*
814 2016;12(2):e1005821.
815 66. Zhang X, Xiao Z, Zhang J, Xu C, Liu S, Cheng L, et al. Differential requirements of IQUB for
816 the assembly of radial spoke 1 and the motility of mouse cilia and flagella. *Cell Rep.*
817 2022;41(8):111683.
818 67. Meng GQ, Wang Y, Luo C, Tan YM, Li Y, Tan C, et al. Bi-allelic variants in DNAH3 cause male
819 infertility with asthenoteratozoospermia in humans and mice. *Hum Reprod Open.*
820 2024;2024(1):hoae003.
821 68. Weng M, Sha Y, Zeng YU, Huang N, Liu W, Zhang X, et al. Mutations in DNAH8 contribute
822 to multiple morphological abnormalities of sperm flagella and male infertility. *Acta Biochim*

Biophys Sin (Shanghai). 2021;53(4):472-80.

Figure Legends

Figure 1. Identification of bi-allelic *DNAH12* variants in infertile men with asthenoteratozoospermia. (A) Pedigrees of family 1 with 3 infertile males, P1 (IV:1), P2 (IV:2), and P3 (IV:4), family 2 with 3 infertile males, P4 (IV:3), P5 (IV:4) and P6 (IV:5), family 3 with 2 infertile males, P7 (IV:1) and P8 (IV:3), and three sporadic infertile cases P9, P10 and P11. Red arrows point to the individuals whom whole-exome sequencing was performed. Candidate mutations were validated by Sanger sequencing and the chromatograms were shown on the right. Red arrowheads point to mutant sites. Double horizontal lines represent consanguineous marriages. WT, wild-type allele; MT, the mutant allele. (B) The positions of the *DNAH12* variants at the transcript (ENST00000351747.2) and protein levels (Q6ZR08-1). MT-like, Microtubule-binding-like domain. (C) Conservation analyses of affected amino acids across different species, the arrowheads indicate the mutation sites.

Figure 2. Abnormal sperm morphology and undetectable DNAH12 expression in men with bi-allelic *DNAH12* variants. (A) Representative micrographs show normal sperm morphology from a fertile control and abnormal spermatozoa from P10 with absent, short, coiled, bent, irregular flagella or abnormal head under light microscopy. Scale bars, 5μm. (B) Representative SEM micrographs show details about the sperm morphology of a fertile control and P10. The normal sperm morphology can be observed in the fertile control (left) and abnormal types like absent, short, coiled, bent, irregular tails, and head abnormality in P10 (right). Scale bars, 5μm. (C) Immunoblotting assay revealed that DNAH12 was absent in the spermatozoa from P9, P10, and P11 harboring *DNAH12* variants. β-actin was used as a loading control. (D) Sperm cells were co-stained with α-Tubulin (green) and DNAH12 (red) antibodies while no DNAH12 signals were observed in sperm flagella of patients. DNA was counterstained with Hoechst 33342. Scale bars, 10μm.

Figure 3. Flagellar axoneme defects were detected in the patients with *DNAH12* variants. (A-B) Representative TEM micrographs showing cross-sections of the midpiece, principal piece, and end piece of sperm flagella from a fertile control and P11. The axoneme structure in control presents a "9+2" microtubules arrangement, including mitochondrial sheath (MS, indicated with red arrows), central pair of microtubules (CP, indicated with yellow arrows), outer dense fibers (ODFs, indicated with cerulean arrows), peripheral doublet microtubules (DMTs, indicated with orange arrows), inner dynein arms (IDAs, indicated with green arrows) and outer dynein arms (ODAs, indicated with purple arrows), while in P11, axonemal defects like missing CP, disorganized axonemal structures or missing DMTs were observed, the red asterisks mark CP loss (A). Impaired IDAs in the sperm axoneme of patient P11 (B). The red triangle marks impaired IDAs while adjacent ODAs are identifiable. Scale bars, 200 nm. (C-D) The proportion of different categories of observed cross-sections in the control and patients. Cross-sections were classified into four categories: Intact "9+2", missing CP, disorganization, and missing DMTs (C), and the proportion of intact IDAs or impaired IDAs in the cross-sections of flagellar axoneme of which ODAs were identifiable (D). n, the total number of cross-sections for quantification. (E-G) Representative images of spermatozoa from fertile controls and patients carrying bi-allelic *DNAH12* variants co-stained α-Tubulin with SPAG6 (E), DNAH1 (F), DNALI1 (G), or DNAH17 (H), and Hoechst 33342 for DNA (blue). Scale bars, 10 μm.

867

868 **Figure 4. Disruption of *Dnah12* results in impaired spermatogenesis and abnormal sperm**
869 **morphology.** (A) Fertility test of adult *Dnah12*$^{+/+}$ and *Dnah12*$^{-/-}$ male mice. (B) The testes to body weight
870 ratios of *Dnah12*$^{+/+}$ *and Dnah12*$^{-/-}$ mice. (C) The number of sperm per epididymis of *Dnah12*$^{+/+}$ *and*
871 *Dnah12*$^{-/-}$ male mice. (D) Percentages of motile sperms in *Dnah12*$^{+/+}$ *and Dnah12*$^{-/-}$ male mice. (E)
872 Histological sections of testis and epididymis from *Dnah12*$^{+/+}$ and *Dnah12*$^{-/-}$ mice after H&E staining.
873 Scale bars, 50 μm. (F) Morphology of the sperm from caudal epididymis of *Dnah12*$^{+/+}$ and *Dnah12*$^{-/-}$
874 mice. Scale bars,10 μm. (G) Quantitative analysis of sperm morphology of *Dnah12*$^{+/+}$ *and Dnah12*$^{-/-}$
875 male mice. The experiments were repeated three times with at least 200 sperms counted every time. The
876 above data were obtained from 3 adult mice for each genotype. (H) Representative images of testicular
877 cells from *Dnah12*$^{+/+}$ and *Dnah12*$^{-/-}$ mice co-stained DNAH12 and α-Tubulin antibodies. Scale bars, 10
878 μm. The red asterisk indicates abnormal manchette structure and the red arrow indicates abnormal sperm
879 flagellum at the elongated spermatid stage of *Dnah12*$^{-/-}$ mice. (I) Representative immunofluorescence
880 images of seminiferous tubule squash from 8-week-old *Dnah12*$^{+/+}$ and *Dnah12*$^{-/-}$ mice, co-stained by
881 PNA (red) and α-Tubulin (green) antibody. DNA was stained with Hoechst 33342. Scale bars, 10 μm.
882 The asterisks indicate the manchette defects and the red triangles mark the abnormal sperm heads. Scale
883 bars,10 μm. (J) Representative TEM micrographs of testicular elongated spermatids from *Dnah12*$^{+/+}$ and
884 *Dnah12*$^{-/-}$ mice. Scale bars, 1μm. (K) TUNEL assay on the testicular sections from *Dnah12*$^{+/+}$ and
885 *Dnah12*$^{-/-}$ mice. The green triangles mark the apoptotic elongating or elongated spermatids. Scale bars,
886 50 μm. (L) The proportion of tubules with apoptotic cells in *Dnah12*$^{+/+}$ and *Dnah12*$^{-/-}$ mice. (M) Average
887 numbers of TUNEL-positive cells per tubule in *Dnah12*$^{+/+}$ and *Dnah12*$^{-/-}$ mice. Data are obtained from
888 three mice with at least 50 tubules scored in each repeated experiment. **$p < 0.01$; ***$p < 0.001$; ****p
889 < 0.0001, Student's t test.
890

891 **Figure 5. Deletion of *Dnah12* causes axoneme defects in mice.** (A) Representative TEM micrographs
892 showing cross-sections of sperm flagella from *Dnah12*$^{+/+}$, *Dnah12*$^{+/-}$, and *Dnah12*$^{-/-}$ mice. In *Dnah12*$^{+/+}$,
893 *Dnah12*$^{+/-}$ groups, the normal axoneme "9+2" microtubule arrangement mainly consisted of the MS,
894 (indicated with red arrows), CP (yellow arrows), ODFs (cerulean arrows), DMTs (orange arrows), IDAs
895 (green arrows) and ODAs (purple arrows). However, the CP and DMTs structures were missing or
896 disarranged in the *Dnah12*$^{-/-}$ group. Red asterisks mark the loss of CP. Scale bars, 200 nm. (B)
897 Immunoblotting of sperm lysate from *Dnah12*$^{+/+}$, *DNAH12*$^{+/-}$ and *Dnah12*$^{-/-}$ mice using DNAH1,
898 DNALI1 or SPAG6 antibodies. DNAI2 and α-Tubulin were used as the loading controls. (C-H)
899 Representative images of caudal epididymal sperm from *Dnah12*$^{+/-}$ and *Dnah12*$^{-/-}$ mice co-stained α-
900 Tubulin and SPAG6 (C), SPEF2 (a component of CP complex) (D), DNAH1 (E), DNALI1 (F), DNAH17
901 (G) or DNAI2 (H) antibodies. Scale bars, 10 μm.
902

903 **Figure 6. DNAH12 interacts with IDA components DNALI1 and DNAH1** (A) Phylogenetic and
904 protein domain analyses of the DNAH family. The dashed box indicates the shortest-length member,
905 DNAH12, while the arrow points to the missing microtubule-binding domain(MTBD) region. (B)
906 Schematic diagram showing the procedure of the immunoprecipitation/mass spectrometry (IP/MS)
907 proteomics experiment. (C) GO term enrichment analysis of DNAH12 potential interactors. (D) Protein-
908 protein interaction network of DNAH12 among the motor protein term. The blue circle marks the
909 proteins involved in IDA assembly. (E-F) Co-IP assays using DNAH12 antibody (E) or DNALI1
910 antibody (F) showed strong and specific interactions among DNAH12, DNALI1, and DNAH1. (G)

Predicted DNAH12-DNALI1 interaction details by the HDOCK server. The top three of DNALI1 possible binding conformations were shown in types 1-3. (H-J) Construction of mouse-mCherry-DNAH12-Stem (H) and mouse-GFP-DNALI1-full length (FL) (I) plasmids, and the validation of the interaction between the Stem domain of DNAH12 and full-length of DNALI1 (J).

Figure 7. DNAH12 facilitates the recruitment of DNALI1 and DNAH1 to flagella, but not cilia (A) Immunoblotting of testis lysate from *Dnah12*$^{+/+}$, *DNAH12*$^{+/-}$ and *Dnah12*$^{-/-}$ mice using DNAH12, DNAH1, and DNALI1 antibodies. DNAI1 (a component of ODAs) and α-Tubulin were used as the loading controls. (B-C) Immunofluorescence assays of α-Tubulin and DNAH1 (B), or DNALI1 (C) antibodies on round spermatids from adult *Dnah12*$^{+/-}$ and *Dnah12*$^{-/-}$ mice. Scale bars, 10 μm. (D-E) Immunofluorescence assays of α-Tubulin and DNAH1 (D), or DNALI1 (E) antibodies on elongated spermatids from adult *Dnah12*$^{+/-}$ and *Dnah12*$^{-/-}$ mice. Scale bars, 10 μm. (F-G) Immunoblotting of oviduct (F) or trachea (G) lysate from *Dnah12*$^{+/+}$, *DNAH12*$^{+/-}$ and *Dnah12*$^{-/-}$ mice using DNAH12, DNAH1, and DNALI1 antibodies. GAPDH was used as the loading control. (H-I) Immunofluorescence assays of the oviduct (H) or trachea (I) sections with α-Tubulin and DNAH1 antibodies. Scale bars, 50 μm. (J-K) Immunofluorescence assays of the oviduct (J) or trachea (K) sections with α-Tubulin and DNALI1 antibodies. Scale bars, 50 μm. (L) Pedigree of a family with 3 infertile males, P12 (III-2), P13 (III:6), and P14 (III:8); MT: the *DNAH1* mutation c.11275C>T; p.Arg3759Cys. (M-O) Representative images of spermatozoa from a fertile control and P13 co-stained by α-Tubulin antibody and DNAH1 (M), DNALI1(N), or DNAH12 (O) antibodies, respectively. Scale bars,10 μm.

Figure 8. DNAH12 may interact with RS head associated proteins to regulate CP stability (A) Co-IP assays of the potential interactions of DNAH12 and RS head proteins RSPH1, RPSH9, or DNAJB13. DNAI2 antibody was used as an negative control. (B) Interaction analyses of DNAH12 and RS head proteins RSPH1, RPSH9, or DNAJB13 by AlphaFold3. (C) Immunoblotting of testis lysate from *Dnah12*$^{+/+}$ and *Dnah12*$^{-/-}$ mice using RSPH1, RPSH9, DNAJB13 antibodies. DNAI2 (a component of ODAs), α-Tubulin and β-Tubulin were used as the loading controls. (D) Immunofluorescence assays of α-Tubulin and RSPH1 antibodies on sperm collected from *Dnah12*$^{+/-}$ and *Dnah12*$^{-/-}$ mice caudal epididymis. Scale bars, 10 μm. (E) Representative two-cell embryos and blastocysts of *Dnah12*$^{+/+}$, and *Dnah12*$^{-/-}$ male mice after intracytoplasmic sperm injection. Scale bar, 100 μm. (F) Percentages of 2-cell-stage embryos of *Dnah12*$^{+/+}$ and *Dnah12*$^{-/-}$ groups. (G) Percentages of blastocyst-stage embryos of *Dnah12*$^{+/+}$ and *Dnah12*$^{-/-}$ groups. (H) Schematic diagram showing the proposed function of DNAH12 in sperm flagellar development in humans and mice. DNAH12 is essential for recruiting DNALI1 and DNAH1 to sperm flagella and maintaining the proper axonemal arrangement, especially IDAs and CP structures. Loss of DNAH12 causes the failure of DNALI1 and DNAH1 to be recruited to sperm flagella and results in abnormal sperm morphology with compromised axoneme organization, causing male infertility. ODA, outer dynein arm; IDA, inner dynein arm; N-DRC, nexin-dynein regulatory complex; CP, central pair of microtubules; MTBD, microtubule-binding domain; RS, radial spoke.

Table 1. Detailed information of bi-allelic *DNAH12* variants identified in infertile men

	Genomic position on chr3	cDNA Change [a]	Mutation type	Genetic pattern	SIFT	Polyphen2	fathmm-MKL	CADD	1000 Genomes	gnomAD
Family 1	57,489,883	MT1: c.944_945del	frameshift substitution	AR	NA	NA	NA	NA	0	0.00002844
Family 2	57,528,434	MT2: c.164A>G	nonsynonymous SNV [b]	Male-limited AR	T	D	D	D	0.000599042	0.0004
Family 3	57,447,323	MT3: c.2560A>G	nonsynonymous SNV	AR	T	D	D	D	0.000599042	0.0002
P9	57,391,670	MT4: c.6229C>T	stop-gain	AR	NA	NA	D	NA	0	0.00002714
P10	57,445,368	MT5: c.2813T>C	nonsynonymous SNV	AR	D	D	D	D	0.000199681	0.00003383
P11	57,394,265	MT6: c. 5964-3A>G	splicing	AR	NA	NA	NA	NA	0.000199681	0.0002
	57,445,501	MT7: c.2680C>T	nonsynonymous SNV		D	D	D	D	0	0.000007178

a. The accession number of human *DNAH12* is ENST00000351747.2. **b.** Abbreviations are listed as follows: SNV, single nucleotide variants; NA, not assessed; T, tolerated; D, deleterious. SIFT, Sorting Intolerant From Tolerant; PolyPhen-2, Polymorphism Phenotype v2; FATHMM-MKL, Functional Analysis Through Hidden Markov Models-Multiple Kernel Learning; CADD, Combined Annotation-Dependent Depletion; and a mutation is predicted deleterious if the CADD Phred score > 20 in CADD. gnomAD, Genome Aggregation Database.

Table 2. Clinical characteristics of the infertile patients with bi-allelic *DNAH12* mutations

	Reference values [a]	Fertile controls [b]	Family1			Family2		Family3	P9	P10	P11
			IV-1(P1)	IV-2(P2)	IV-4(P3)	IV-5(P4)	IV-7(P5)	IV-4(P8)			
cDNA mutation	–	–	MT1/MT1	MT1/MT1	MT1/MT1	MT2/MT2	MT2/MT2	MT3/MT3	MT4/MT4	MT5/MT5	MT6/MT7
Age (y) [c]	–	–	58	49	42	40	38	32	33	40	31
Semen parameters											
Semen volume (ml)	>1.5	–	ND	1.5±0.5	2.8±0.3	4.0	3.0	3.0	3.2	3.1	2.4
Sperm concentration (10^6/ml)	>15	–	ND	58±28.5	50.0±15.0	6.0	8.0	2.8	24.7	83.1	57.1
Semen pH	Alkaline	–	ND	Alkaline	Alkaline	Alkaline	Alkaline	Alkaline	Alkaline	Alkaline	Alkaline
Motile sperm (%)	>40	–	ND	29.3±9.0	7.5±7.5	14.0	20.0	20	15.1	17.4	7.4
Progressively motile sperm (%)	>32	–	ND	13.3±10.3	16.7±17	5.0	8.0	5	13.4	16.8	24
Sperm morphology											
Normal (%)	–	76.5±2.0	ND	ND	19.9 [d]	ND	21.7	17.0	14.0	17.4	7.4
Abnormal head (%)	–	7.0±1.9	ND	ND	16.4	ND	5.4	6.0	3.5	16.4	20.0
Abnormal tail (%)	–	12.4±3.4	ND	ND	43.8	ND	41.4	44.0	42.4	37.4	16.3
Abnormal head &tail (%)	–	4.1±1.3	ND	ND	19.9	ND	31.5	33.0	40.2	28.8	56.3
Sperm flagella morphology											
Normal (%)	–	83.1±2.3	ND	ND	26.4	ND	26.6	22.7	17.9	31.7	27.4
Absent (%)	–	2.7±1.1	ND	ND	16.4	ND	7.9	15.8	9.6	16.6	11.6
Short (%)	–	3.6±0.6	ND	ND	16.4	ND	11.3	14.9	20.1	11.7	8.4
Coiled (%)	–	2.8±0.7	ND	ND	17.3	ND	24.6	12.9	11.8	14.6	7.0
Bent (%)	–	6.3±0.6	ND	ND	12.7	ND	15.8	10.0	13.5	7.8	33.5
Irregular caliber (%)	–	1.5±0.2	ND	ND	10.9	ND	13.8	23.8	27.1	17.6	12.1

a. The reference limits are shown according to WHO 6th edition standards. **b.** Reference values are shown by observation of sperm morphology in 3 fertile individuals. **c.** "Age" represents age in 2024. ND, not determined. **d.** Values in red colors show obvious declined proportions of normal sperm morphology compared with fertile controls.

Figure 1

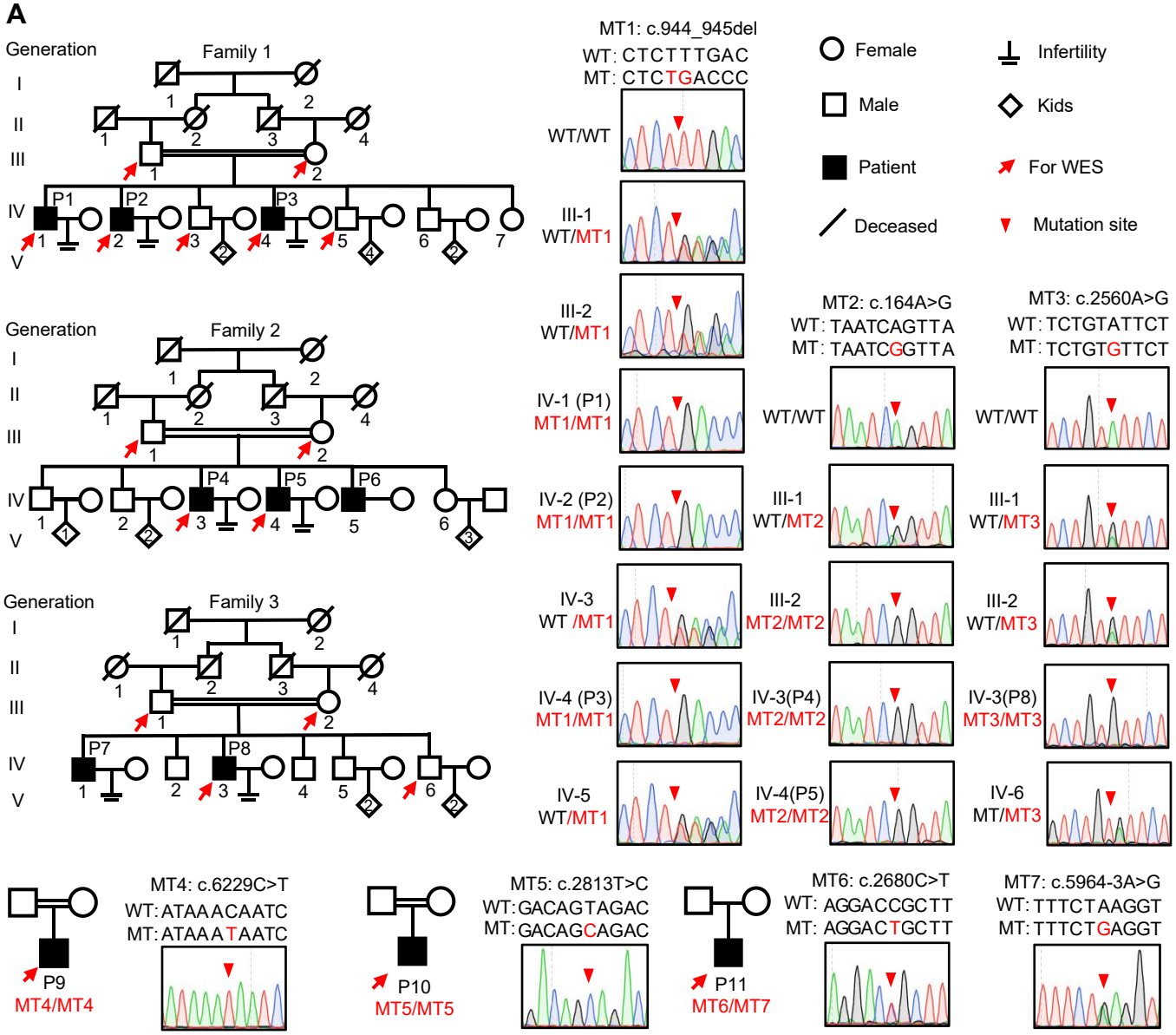
A
Generation
Family 1
I
II
III
IV
V
P1
P2
P3
Family 2
P4
P5
P6
Family 3
P7
P8
MT1: c.944_945del
WT: CTCTTTGAC
MT: CTCTGACCC
WT/WT
III-1
WT/MT1
III-2
WT/MT1
IV-1 (P1)
MT1/MT1
IV-2 (P2)
MT1/MT1
IV-3
WT /MT1
IV-4 (P3)
MT1/MT1
IV-5
WT/MT1
Female
Male
Patient
Deceased
Infertility
Kids
For WES
Mutation site
MT2: c.164A>G
WT: TAATCAGTTA
MT: TAATCGGTTA
WT/WT
III-1
WT/MT2
III-2
MT2/MT2
IV-3(P4)
MT2/MT2
IV-4(P5)
MT2/MT2
MT3: c.2560A>G
WT: TCTGTATTCT
MT: TCTGTGTTCT
WT/WT
III-1
WT/MT3
III-2
WT/MT3
IV-3(P8)
MT3/MT3
IV-6
MT/MT3
P9
MT4/MT4
MT4: c.6229C>T
WT: ATAAACAATC
MT: ATAAATAATC
P10
MT5/MT5
MT5: c.2813T>C
WT: GACAGTAGAC
MT: GACAGCAGAC
P11
MT6/MT7
MT6: c.2680C>T
WT: AGGACCGCTT
MT: AGGACTGCTT
MT7: c.5964-3A>G
WT: TTTCTAAGGT
MT: TTTCTGAGGT
B
MT2
c.164A>G
MT1
c.944_945del
MT3
c.2560A>G
MT6
c.2680C>T
MT5
c.2813T>C
MT7
c.5964-3A>G
MT4
c.6229C>T
DNAH12
MT2
p.Gln55Arg
MT1
p.Phe315*
MT3
p.Ile854Val
MT6
p.Arg894Cys
MT5
p.Val938Ala
MT4
p.Gln2077*
DNAH12
Protein
Stem
AAA 1
AAA 2
AAA 3
AAA 4
MT-like
AAA 5
1
1000
2000
3092
C
MT2: p.Gln55Arg
MT1: p.Phe315*
MT3: p.Ile854Val
MT6: p.Arg894Cys
MT5: p.Val938Ala
MT4: p.Gln2077*
Human
Chimpanzee
Pig
Mouse
Rat
Cat
Goat

Figure 2

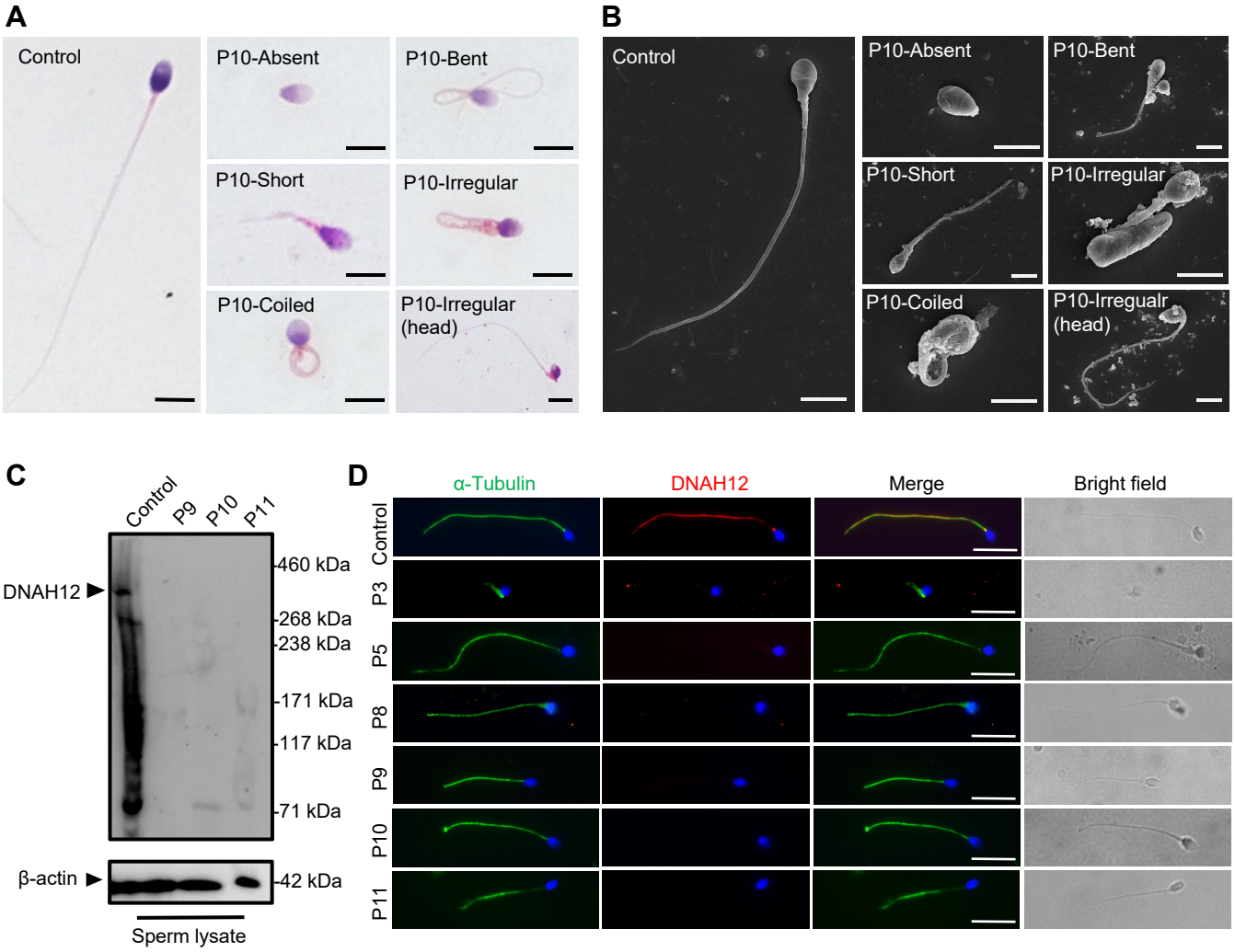
A
Control
P10-Absent
P10-Bent
P10-Short
P10-Irregular
P10-Coiled
P10-Irregular (head)
B
Control
P10-Absent
P10-Bent
P10-Short
P10-Irregular
P10-Coiled
P10-Irregualr (head)
C
Control
P9
P10
P11
DNAH12
460 kDa
268 kDa
238 kDa
171 kDa
117 kDa
71 kDa
β-actin
42 kDa
Sperm lysate
D
α-Tubulin
DNAH12
Merge
Bright field
Control
P3
P5
P8
P9
P10
P11

Figure 3

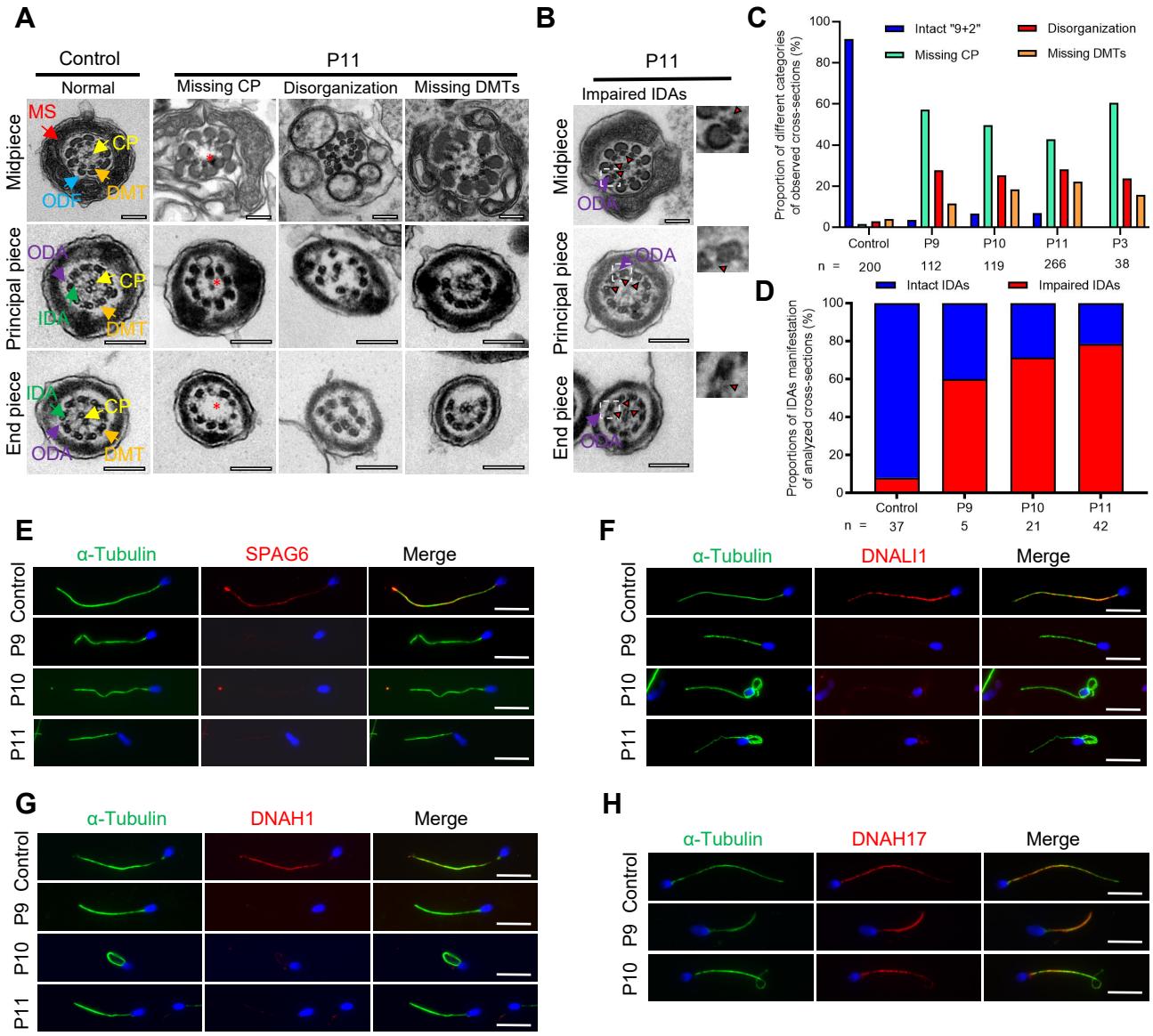
A
Control
P11
Normal
Missing CP
Disorganization
Missing DMTs
Midpiece
Principal piece
End piece
MS
CP
ODF
DMT
ODA
IDA
B
P11
Impaired IDAs
C
Intact "9+2"
Disorganization
Missing CP
Missing DMTs
Proportion of different categories of observed cross-sections (%)
Control
P9
P10
P11
P3
n = 200 112 119 266 38
D
Intact IDAs
Impaired IDAs
Proportions of IDAs manifestation of analyzed cross-sections (%)
n = 37 5 21 42
E
α-Tubulin
SPAG6
Merge
F
DNALI1
G
DNAH1
H
DNAH17

Figure 4

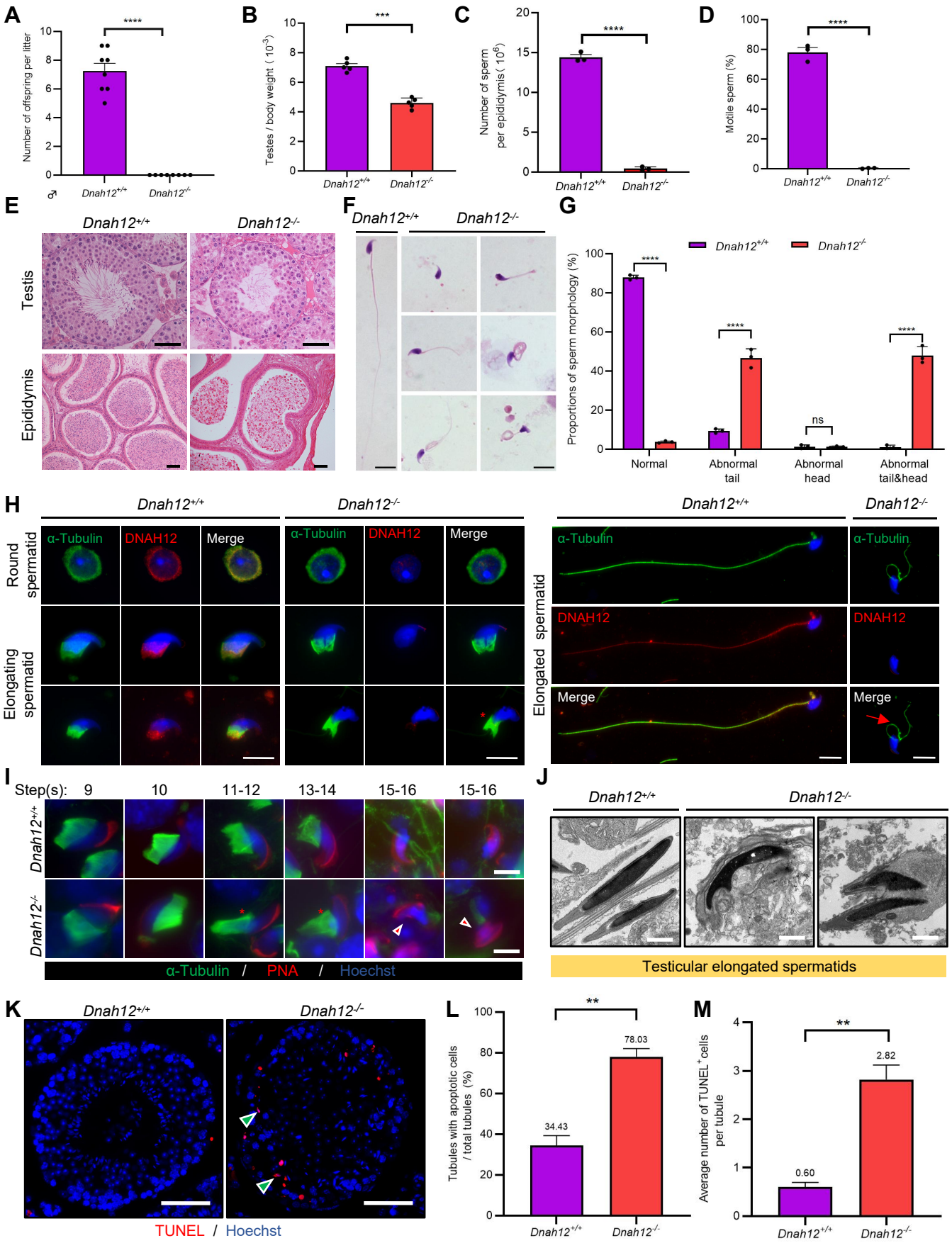
A
Number of offspring per litter
♂
Dnah12+/+
Dnah12-/-
B
Testes / body weight (10-3)
C
Number of sperm per epididymis (106)
D
Motile sperm (%)
E
Testis
Epididymis
F
G
Proportions of sperm morphology (%)
Normal
Abnormal tail
Abnormal head
Abnormal tail&head
ns
H
Round spermatid
Elongating spermatid
Elongated spermatid
α-Tubulin
DNAH12
Merge
I
Step(s): 9 10 11-12 13-14 15-16 15-16
α-Tubulin / PNA / Hoechst
J
Testicular elongated spermatids
K
TUNEL / Hoechst
L
Tubules with apoptotic cells / total tubules (%)
34.43
78.03
M
Average number of TUNEL+ cells per tubule
0.60
2.82

Figure 5

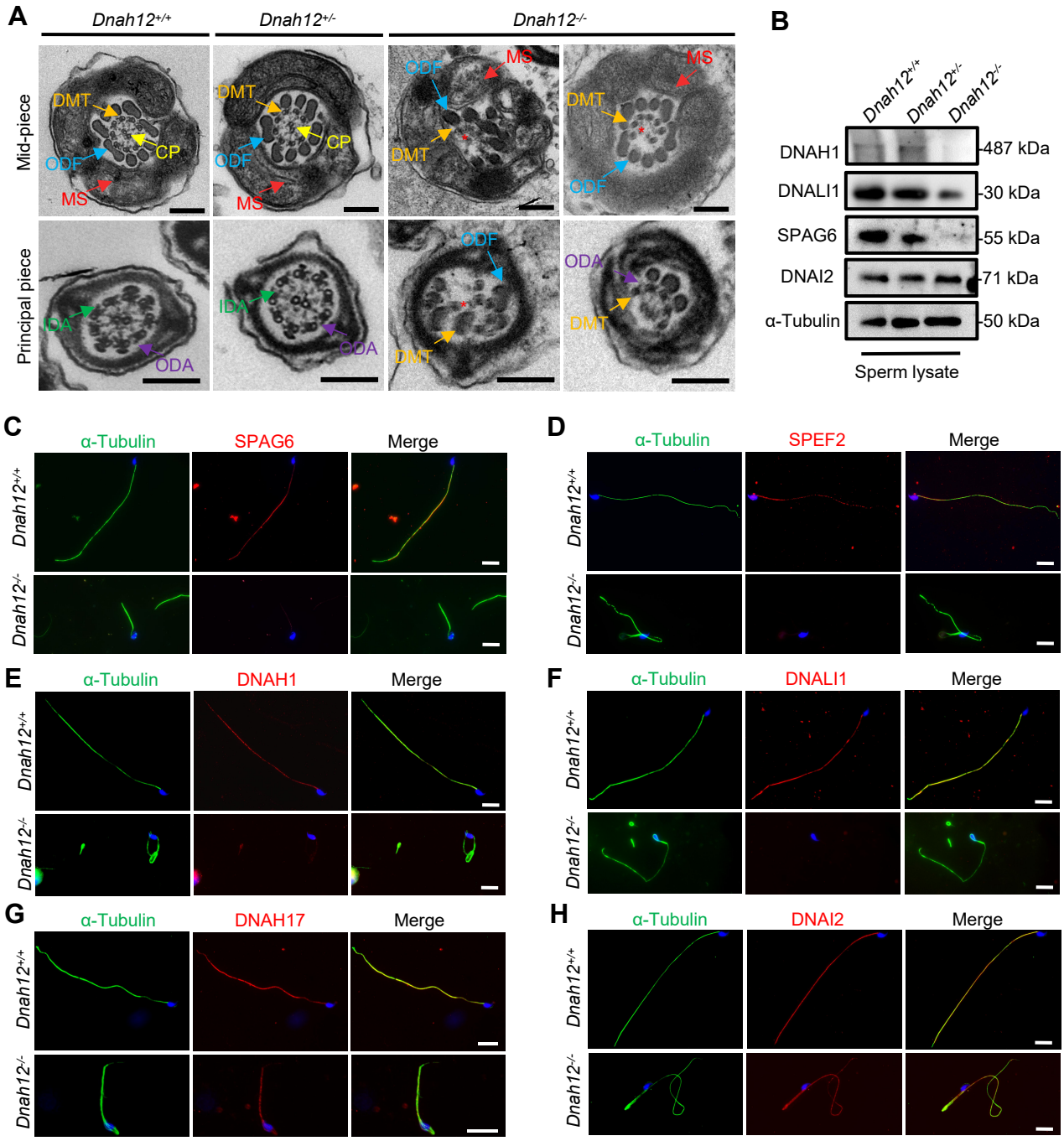
A
Dnah12+/+
Dnah12+/-
Dnah12-/-
Mid-piece
Principal piece
DMT
CP
ODF
MS
IDA
ODA
B
Dnah12+/+
Dnah12+/-
Dnah12-/-
DNAH1
DNALI1
SPAG6
DNAI2
α-Tubulin
487 kDa
30 kDa
55 kDa
71 kDa
50 kDa
Sperm lysate
C
α-Tubulin
SPAG6
Merge
D
SPEF2
E
DNAH1
F
DNALI1
G
DNAH17
H
DNAI2

Figure 6

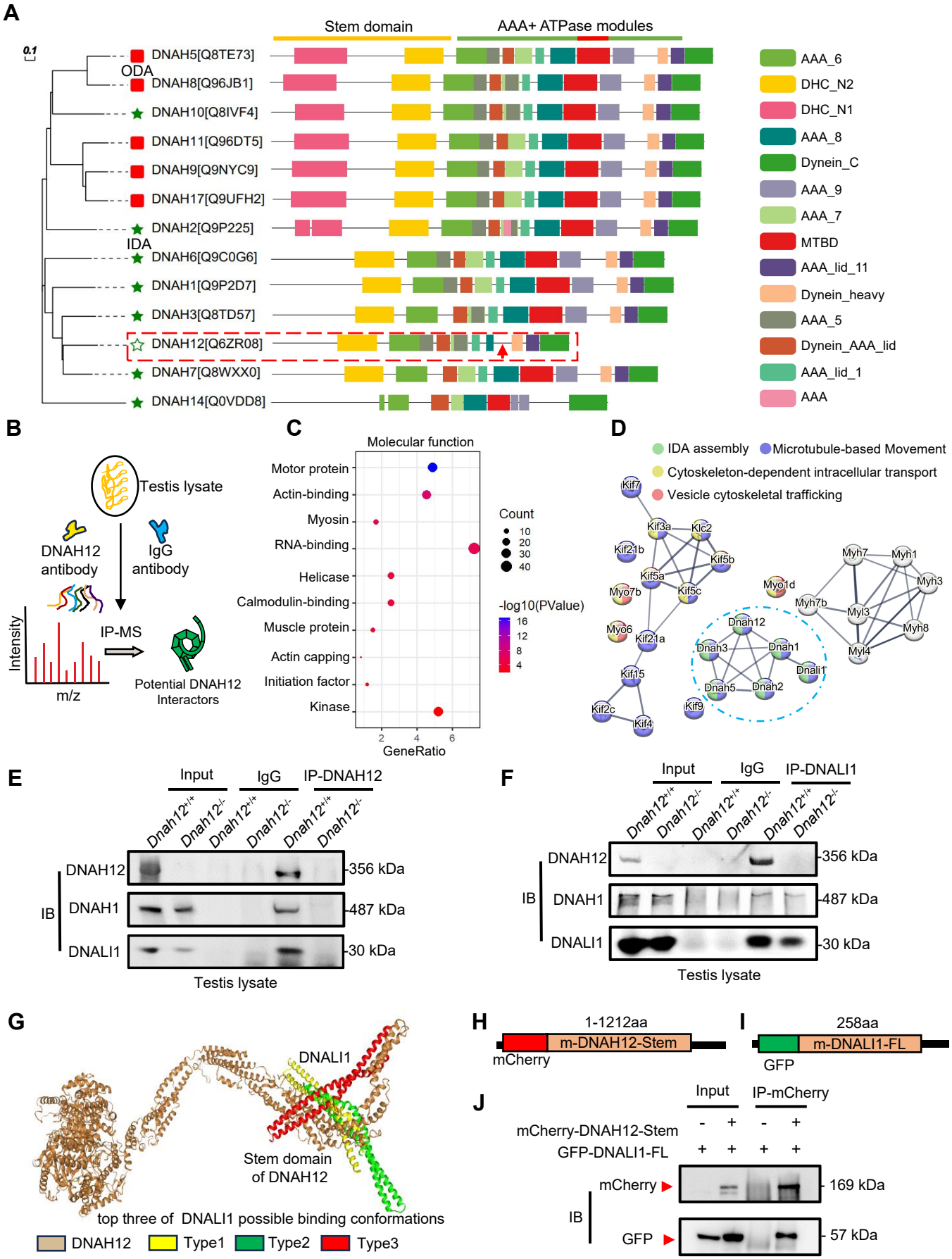
A
Stem domain
AAA+ ATPase modules
0.1
ODA
IDA
DNAH5[Q8TE73]
DNAH8[Q96JB1]
DNAH10[Q8IVF4]
DNAH11[Q96DT5]
DNAH9[Q9NYC9]
DNAH17[Q9UFH2]
DNAH2[Q9P225]
DNAH6[Q9C0G6]
DNAH1[Q9P2D7]
DNAH3[Q8TD57]
DNAH12[Q6ZR08]
DNAH7[Q8WXX0]
DNAH14[Q0VDD8]
AAA_6
DHC_N2
DHC_N1
AAA_8
Dynein_C
AAA_9
AAA_7
MTBD
AAA_lid_11
Dynein_heavy
AAA_5
Dynein_AAA_lid
AAA_lid_1
AAA
B
Testis lysate
DNAH12 antibody
IgG antibody
IP-MS
Intensity
m/z
Potential DNAH12 Interactors
C
Molecular function
Motor protein
Actin-binding
Myosin
RNA-binding
Helicase
Calmodulin-binding
Muscle protein
Actin capping
Initiation factor
Kinase
GeneRatio
Count
-log10(PValue)
D
IDA assembly
Microtubule-based Movement
Cytoskeleton-dependent intracellular transport
Vesicle cytoskeletal trafficking
Kif7
Kif3a
Klc2
Kif21b
Kif5b
Kif5a
Myo7b
Kif5c
Myo6
Kif21a
Kif15
Kif2c
Kif4
Myo1d
Myh7
Myh1
Myh3
Myh7b
Myl3
Myh8
Myl4
Dnah12
Dnah3
Dnah1
Dnali1
Dnah5
Dnah2
Kif9
E
Input
IgG
IP-DNAH12
Dnah12+/+
Dnah12-/-
IB
DNAH12
DNAH1
DNALI1
356 kDa
487 kDa
30 kDa
Testis lysate
F
Input
IgG
IP-DNALI1
Dnah12+/+
Dnah12-/-
IB
DNAH12
DNAH1
DNALI1
356 kDa
487 kDa
30 kDa
Testis lysate
G
DNALI1
Stem domain of DNAH12
top three of DNALI1 possible binding conformations
DNAH12
Type1
Type2
Type3
H
1-1212aa
m-DNAH12-Stem
mCherry
I
258aa
m-DNALI1-FL
GFP
J
Input
IP-mCherry
mCherry-DNAH12-Stem
GFP-DNALI1-FL
IB
mCherry
GFP
169 kDa
57 kDa

Figure 7

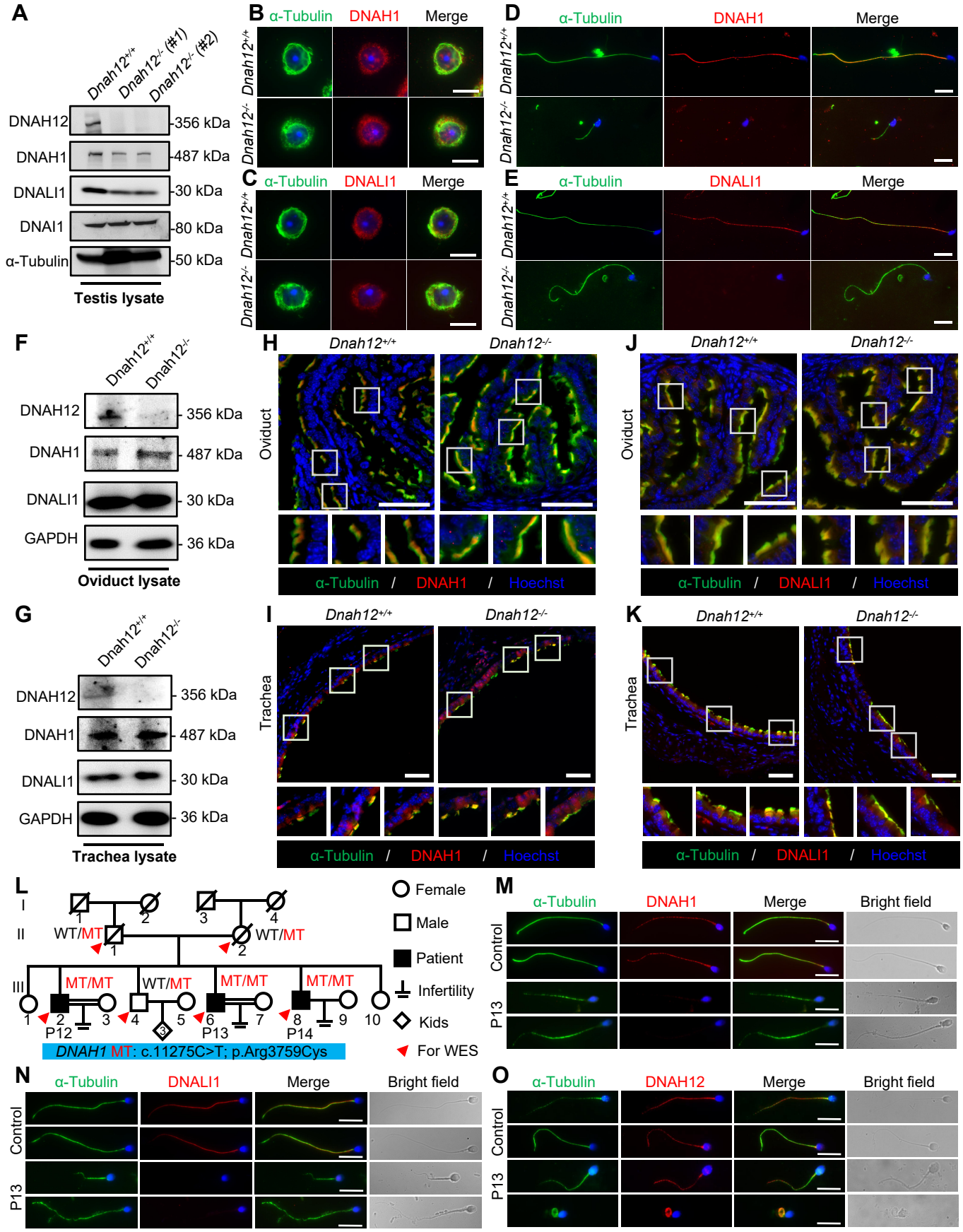
A
Dnah12+/+
Dnah12-/- (#1)
Dnah12-/- (#2)
DNAH12
DNAH1
DNALI1
DNAI1
α-Tubulin
356 kDa
487 kDa
30 kDa
80 kDa
50 kDa
Testis lysate
B
α-Tubulin
DNAH1
Merge
C
DNALI1
D
E
F
Oviduct lysate
G
Trachea lysate
H
Dnah12+/+
Dnah12-/-
Oviduct
α-Tubulin / DNAH1 / Hoechst
I
Trachea
J
α-Tubulin / DNALI1 / Hoechst
K
L
WT/MT
MT/MT
P12
P13
P14
DNAH1 MT: c.11275C>T; p.Arg3759Cys
Female
Male
Patient
Infertility
Kids
For WES
M
Bright field
Control
N
O
DNAH12

Figure 8

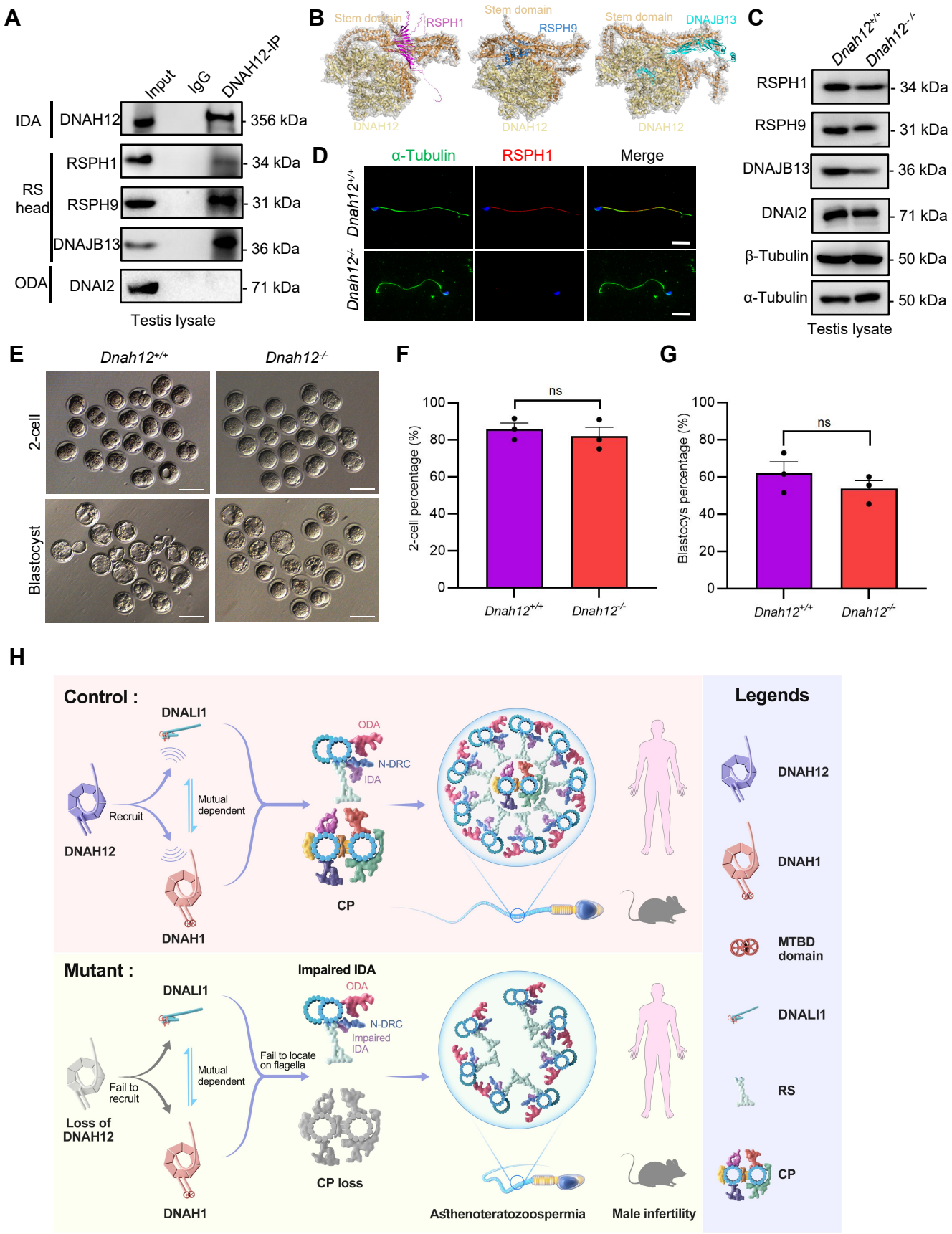
A
Input
IgG
DNAH12-IP
IDA
DNAH12
356 kDa
RS head
RSPH1
34 kDa
RSPH9
31 kDa
DNAJB13
36 kDa
ODA
DNAI2
71 kDa
Testis lysate
B
Stem domain
RSPH1
RSPH9
DNAJB13
DNAH12
C
Dnah12+/+
Dnah12-/-
RSPH1
34 kDa
RSPH9
31 kDa
DNAJB13
36 kDa
DNAI2
71 kDa
β-Tubulin
50 kDa
α-Tubulin
50 kDa
Testis lysate
D
α-Tubulin
RSPH1
Merge
Dnah12+/+
Dnah12-/-
E
Dnah12+/+
Dnah12-/-
2-cell
Blastocyst
F
ns
2-cell percentage (%)
100
80
60
40
20
0
Dnah12+/+
Dnah12-/-
G
ns
Blastocys percentage (%)
100
80
60
40
20
0
Dnah12+/+
Dnah12-/-
H
Control :
DNALI1
Recruit
Mutual dependent
DNAH12
DNAH1
ODA
N-DRC
IDA
CP
Mutant :
DNALI1
Fail to recruit
Mutual dependent
Loss of DNAH12
DNAH1
Impaired IDA
ODA
N-DRC
Impaired IDA
Fail to locate on flagella
CP loss
Asthenoteratozoospermia
Male infertility
Legends
DNAH12
DNAH1
MTBD domain
DNALI1
RS
CP